



Contents lists available at ScienceDirect

International Journal of Plasticity

journal homepage: www.elsevier.com/locate/ijplas



Irradiation hardening behavior of high entropy alloys using random field theory informed discrete dislocation dynamics simulation

Yang Chen ^{a,1}, Shuo Wang ^{a,1}, Hui Feng ^a, Weipeng Li ^{a,*}, Bin Liu ^b, Jia Li ^{a,*}, Yong Liu ^b, Peter K. Liaw ^c, Qihong Fang ^{a,*}

^a State Key Laboratory of Advanced Design and Manufacturing for Vehicle Body, College of Mechanical and Vehicle Engineering, Hunan University, Changsha, 410082, Hunan, PR China

^b State Key Laboratory of Powder Metallurgy, Central South University, Changsha, 410083, Hunan, PR China

^c Department of Materials Science and Engineering, The University of Tennessee, Knoxville, TN 37996, USA



ARTICLE INFO

Keywords:

High entropy alloys
Irradiation hardening
Transmission electron microscopy
Discrete dislocation dynamics
Dislocation loop
Heterogeneous lattice strain

Article Info

High entropy alloys (HEAs) exhibit outstanding radiation resistance over traditional alloys owing to severe lattice distortion, and therefore, would be regarded as candidate materials for advanced reactors. However, the complex evolution of dislocation configurations in the irradiated HEAs subjected to the external loads has not been uncovered at the micron scale. To elucidate this key mechanism, we develop the random field theory informed discrete dislocation dynamics simulations based on high-resolution transmission electron microscopy, to systematically clarify the role of heterogeneous lattice strain on the complex interactions between the dislocation loop and dislocation in three-dimensional (3D) space. The results show that the lattice-strain-induced irradiation hardening decreases, in agreement with the excellent irradiation hardening resistance of the HEAs from the recent experiment. Based on the analysis of the micrometer-scale dislocation multiplication process, a new cross-slip mechanism through the collinear reaction between dislocations and rhombus perfect loops is revealed. The peaks and valleys of the heterogeneous lattice strains induced by severe lattice distortion are randomly distributed in a 3D space, reducing an aggregation of lattice point and dislocation density at the local region. The cross-slip process occurs by the joint action of the lattice distortion and rhombus-perfect-loop dislocation reaction, leading to the strong irradiation resistance attributed to a large number of narrow defect-free channel under a relatively random strain localization. The present study gives an insight into the fundamental irradiation damage behavior at the mesoscopic scale, thereby guiding the development of advanced HEA materials through the regulation of heterogeneous lattice strain for nuclear energy applications.

1. Introduction

The conflict between the rapid economic development and the goal of “carbon peak and carbon neutralization” has become increasingly prominent (Cheng et al., 2022; Pitike et al., 2022). Now, fossil fuels are still one of the most important energies but bring a series of serious environmental pollution problems. Therefore, it is urgent to develop new energy, such as solar energy, nuclear energy, wind energy, tide, geothermal source, and others. As one of the most widely used new energy in the present world,

* Corresponding authors.

E-mail addresses: liweipeng@hnu.edu.cn (W. Li), lijia123@hnu.edu.cn (J. Li), fangqh1327@hnu.edu.cn (Q. Fang).

¹ These authors contributed equally to this work.

nuclear energy has some advantages of pollution-free, high-energy density and low comprehensive cost (Natarajan et al., 2020; Zhang et al., 2021). However, the challenging environment of a nuclear reactor contains not only extreme temperatures, stress, and corrosion, but also high levels of ion and neutron radiation for advanced nuclear-power stations (Ren et al., 2020).

High entropy alloys (HEAs) are a new type of alloy composed of five or more elements with equal or nearly-equal amounts of elemental concentrations. Thus, HEAs have high mixing entropy, and leads to low Gibbs free energy, making them more likely to form stable solid solutions rather than complex intermetallic compounds (Jiang et al., 2020; Li et al., 2020; Peng et al., 2021; Zhang et al., 2022). Besides, the differences in atomic radii of elements cause the lattice distortion in HEAs, which can improve the solid solubility of interstitial atoms, thus promoting the solid solution strengthening of materials (Chen et al., 2020c; Lei et al., 2018; Li et al., 2021a; Pan et al., 2021; Shi et al., 2021). Therefore, HEAs have outstanding properties, such as high strength, high hardness, great corrosion resistance, and excellent high temperature resistance (Xin et al., 2022). In addition, due to the complex elemental compositions and the unique cocktail effects, HEAs are extremely promising to optimize the composition in a wide range for obtaining an excellent irradiation resistance (Feng et al., 2021; Pickering et al., 2021; Tunes et al., 2021). Consequently, HEAs have been considered promising application materials in the nuclear-power plants in recent years (Huang et al., 2022; Su et al., 2022).

HEAs have drawn extensive interest of researchers in the field of nuclear materials due to their excellent mechanical properties under harsh environments and great potential in irradiation resistance (Aizenshtein et al., 2020; Barr et al., 2018; Yang et al., 2018). Compared with the commercial 304SS and pure Ni, the He bubble produced after high temperature irradiation is smaller in the FeCoCrNiMn HEA, and the mobility of He atoms and point defects is lower. This result indicates that HEAs have a more stable structure after irradiation (Yang et al., 2019). In addition, the FeCoCrNi HEAs have a higher defect recombination rate than that of a pure Ni (Lin et al., 2020), indicating their high radiation resistance. The irradiation behavior of the FeNiMnCr HEA at the temperature ranging from 300 °C to 700 °C with doses of 0.1–10 dpa shows higher phase stability and lower degree of radiation-induced solute segregation at grain boundaries than that of the austenitic alloys (Kumar et al., 2016). A refractory HfTaTiVZr HEA with low activation constituent elements is developed (Sadeghilaridjani et al., 2020). The irradiation-hardening rate is 30% lower than that of the stainless steel under the same irradiation conditions, attributed to the reduced defect mobility and the self-healing ability. The carbon doping at room temperature reduces the size of dislocation loops and the hardening rate in the carbon doped HEAs, owing to the increase of the lattice distortion, migration energy of self-interstitial atoms, and the resistance of carbon atoms to the defect evolution (Shen et al., 2020). In the series of experimental research, the excellent irradiation resistance of HEAs usually depends on the high level of lattice distortion and the hysteresis diffusion, which improve the formation energies of voids. This trend would increase the migration barriers of defects introduced by irradiation, thus reducing the dislocation size and density and alleviating the deterioration of material properties (Chen et al., 2018; Zhao et al., 2022).

The modeling and simulations of the irradiation properties of HEAs are also being conducted to further explore the internal mechanism of their excellent irradiation resistance (Deluigi et al., 2021; Fang et al., 2021; Zhang et al., 2022). The formation of vacancy clusters related to the irradiation resistance is studied in the FeCoCrNiMn HEA based on first-principles calculations. It reveals that the excellent irradiation resistance of FeCoCrNiMn HEA is originated from few stable tri-vacancy clusters (Xu et al., 2021). The primary irradiation damage of the FeCoCrNiCu HEA is studied by combining experiments and molecular dynamics (MD) simulations. The origin of the radiation resistance of HEAs observed in the experiments might not be related to the reduction of the primary irradiation damage caused by chemical disorder, but rather caused by the longer-time defect evolution (Deluigi et al., 2021). Combined with transmission electron microscopy (TEM) and MD simulations, the behavior of He bubble in the FeCoCrNi HEAs after the irradiation is studied. The addition of elements promotes the displacement and diffusion of He, thus promoting the growth of He bubbles and reducing their nucleation (Chen et al., 2020b).

A large number of irradiation experiments have shown that the radiation hardening rates of HEAs are lower than those of conventional alloys (El-Atwani et al., 2019; Jin et al., 2016; Li et al., 2019a; Sadeghilaridjani et al., 2020; Zhang et al., 2021), indicating their better irradiation hardening behavior. The lower radiation hardening is usually attributed to the small size and density of radiation defects in HEAs induced by the severe lattice distortion and diffusion hysteresis (El-Atwani et al., 2019; Yang et al., 2019). However, there are few studies to reveal the radiation hardening mechanism of HEAs from the perspective of the radiation-defect hindering dislocation motion at the mesoscopic scale. Fig. 1 shows that the traditional alloys have relatively symmetrical lattice structure and low lattice strain; however, the HEAs have severely distorted lattice structure and high lattice strain. This result would cause the significant change in the dislocation-based damage mechanism and defect-free channel distribution, thus leading to the low radiation-hardening behavior in the HEAs (Lu et al. (2016)). As we all know, the severe lattice distortion-induced stress field unique to HEAs makes the dislocation motion unusual, compared to the conventional alloys (Chen et al., 2020a; Li et al., 2019b; Ma, 2020), which seriously affects the interaction process of dislocations and irradiation defects. Therefore, it is necessary to investigate the influence of a large number of dislocation motions, collisions and reactions with radiation defects on radiation hardening under the action of heterogeneous lattice distortion at the mesoscopic scale.

2. Experiment

2.1. Sample preparation

The FeCoCrNi HEA samples with an equal atomic ratio were prepared by vacuum induction melting. The raw material was the elemental metal powder with purity of at least 99.9 weight percent (wt%), and the mass ratio of each element is calculated according to the atomic ratio of each element. The as-cast FeCoCrNi HEA was smelted under vacuum in a high purity argon atmosphere according to the calculated mass ratios of each component. To ensure the uniformity of the various elements, each sample was reversed and remelted six times and homogenized at 1273 K for 12 h.

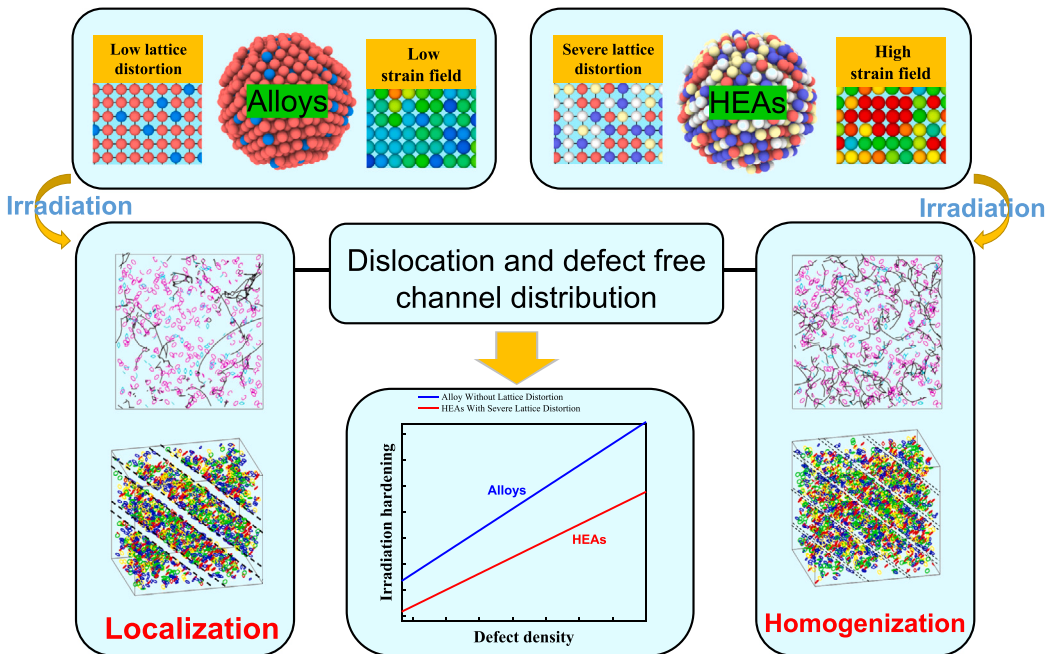


Fig. 1. Schematic diagram for the comparison of irradiation damage mechanism in alloys and HEAs.

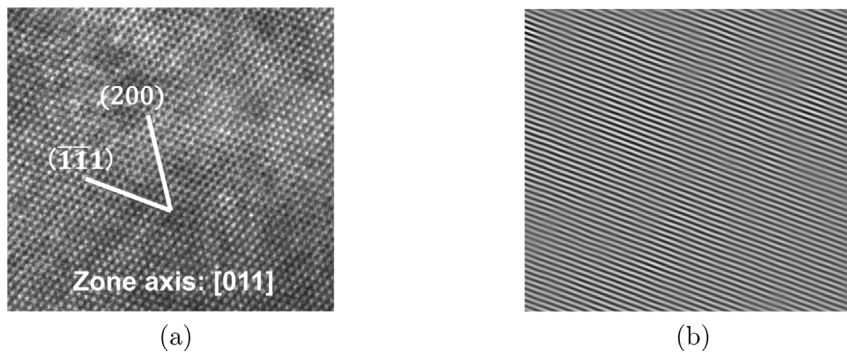


Fig. 2. (a) The high-resolution transmission electron microscopy (TEM) image with the [011] zone axis. (b) The filtered inverse FFT image of $\langle\bar{1}\bar{1}1\rangle$ plane in (a).

2.2. Characterization method

The wire-cut FeCoCrNi HEA samples were mechanically polished with SiC sandpaper to a thickness about 50 μm . Subsequently, the thin sheet was punched into disks with a diameter of 3 mm, followed by mechanically dimpling. Then, the TEM samples were ion milled, using Gatan PIPS, Model 695 to a thickness of electron transparency. The high-resolution transmission electron microscopy (HRTEM) experiment was performed in a JEOL JEM 2100F microscope. The geometric phase analysis (GPA) was conducted via the open source program Strain ++ (Hýtch et al., 1998).

2.3. Fractal function

In recent years, the lattice distortion of HEAs has been directly measured using the experimental methods (Owen and Jones, 2018). Among them, the GPA methods based on the TEM experiments have been widely adopted to characterize the lattice strain in HEAs (Ding et al. (2019), Chen et al. (2021)). Here, the lattice strain of the FeCoCrNi model alloy was characterized by GPA based on the lattice image from the TEM experiments (Hýtch et al., 1998). Figure 2(a) shows the lattice image of the FeCoCrNi HEAs. Figure 2(b) presents the filtered inverse fast Fourier transformation (FFT) image. Figure 2(b) indicates that the area observed by TEM is from the defect-free region of an undeformed FeCoCrNi HEA (Li et al., 2022). Therefore, the lattice strain fields obtained based on GPA are entirely derived from severe atomic lattice distortions.

Recent researches show that the experimentally measured residual strain is consistent with the fractal distribution in HEAs (Li et al. (2022)). Here, a multivariable Weierstrass–Mandelbrot (W–M) function is applied to describe lattice strain fields with randomness in 3D space (Ausloos and Berman, 1985).

$$W(\mathbf{r}) = \left(\frac{\ln \gamma}{M} \right)^{\frac{1}{2}} \sum_{m=1}^M \sum_{n=-\infty}^{\infty} A_m [\cos(\phi_{m,n}) - \cos(k_0 \gamma^n \vec{n}_m \cdot \mathbf{r} + \phi_{m,n})] (k_0 \gamma^n)^{D-4} \quad (1)$$

where $(\ln \gamma / M)^{\frac{1}{2}}$ is the normalizing factor, M is the number of superposed ridges, A_m is the amplitude, $A_m = (2\pi)^{4-D} H^{D-3}$ is chosen to obtain an isotropic 3D strain field function, H is the strain amplitude, $\phi_{m,n}$ is an arbitrary phase, and D is the fractal dimension. $k_0 = 2\pi/L$ indicates the wave number, which is used to scale horizontal variability, and L is the sample size selected in the experimental measurement of the strain field. n is the frequency index, which is a finite size value related to the sample size. The maximum value of n is given by $\gamma^n = L/L_s$, where $L_s = 4b$ is a cutoff length. γ is a constant related to the frequency density of the strain wave. $\gamma = 1.5$ is applied, considering the surface flatness and frequency distribution density of the generated strain field. $M = 50$ is the number of superimposed ridges of the generated strain field profile. Then, the 3D strain field function can be expressed as

$$\epsilon(\mathbf{r}) = H^{D-3} \left(\frac{\ln \gamma}{M} \right)^{\frac{1}{2}} \sum_{m=1}^M \sum_{n=0}^{n_{\max}} \left[\cos(\phi_{m,n}) - \cos\left(\frac{2\pi \gamma^n \vec{n}_m \cdot \mathbf{r}}{L} + \phi_{m,n}\right) \right] \left(\frac{\gamma^n}{L}\right)^{D-4} \quad (2)$$

where \vec{n}_m is the unit vectors distributed uniformly spaced on a unit 3D hypersphere. The corresponding 3D stress field is obtained by the application of the generalized Hooke's law $\sigma_{ij} = 2G\epsilon_{ij} + \lambda\epsilon_{kk}\delta_{ij}$, where G and λ are the shear modulus and Lame coefficient, respectively.

It is significant to emphasize that the variation of the amplitude causes the anisotropy of the surface of the strain field. The present DDD package is only available for simulations based on the isotropic assumption, although the calculation results from DDD simulations are widely accepted (Fan et al., 2021; Shih et al., 2021). Therefore, an average value of a strain field, $\bar{\epsilon}$, is subtracted by the 3D heterogeneous strain field fractal function to eliminate the influence of the anisotropy. $\bar{\epsilon}$ is calculated by $100 \times 100 \times 100$ uniformly distributed discrete points in simulation box, and $\bar{\epsilon} = \sum_k \sum_m \sum_n \epsilon(x_k, y_m, z_n, H, D, \phi_{m,n}) / 10^6 (k, m, n = 1 \dots 100)$.

2.4. Structure function method

Based on the structure-function method (Li et al., 2022), the corresponding fractal dimension and strain amplitude of a 3D fractal function for different strain components of the FeCoCrNi HEA are obtained from the experiment (Fig. 3). The structure function in 3D space is defined as (Li et al., 2022; Zhang et al., 2017):

$$S(\tau_x, \tau_y) = \langle (z(x, y) - z(x + \tau_x, y + \tau_y))^2 \rangle \quad (3)$$

where $\tau_x = L_{\text{hori}} \cos \theta$ and $\tau_y = L_{\text{hori}} \sin \theta$ are the spatial lag between the discrete point (x, y) and its delayed copy $(x + \tau_x, y + \tau_y)$. L_{hori} represents the horizontal distance. $z(x, y)$ is the strain experimentally measured form TEM and GPA. $\langle \dots \rangle$ indicates the space average value of the expressions inside it. θ is the uniformly distributed discrete values between 0 and 2π .

There is an approximate scaling-law behavior in the profile of the structure function derived from the image:

$$S(L_{\text{hori}}) = A(L_{\text{hori}})^{2(2-D_s)} \quad (4)$$

where $D_s = (4 - T_s)/2$ is the fractal dimension of profile, T_s and $\ln(A)$ are obtained from the slope and intercept of the logarithmic diagram of S and L_{hori} . The strain amplitude, H , is calculated as:

$$H = \left[-\frac{2}{\pi} A \Gamma(5 - 2D_s) \sin(\pi D_s) \right]^{1/(2D_s - 2)} \quad (5)$$

The fractal dimension of strain field is $D = \langle D_s \rangle + 2$. The calculation results of the fractal dimension and strain amplitude are listed in Table 1. The statistical comparison of the normal and shear strains between the fractal function and experimental result with the resolution of 0.1 nm shows the same spacing between the strain peaks and valleys (Fig. 3), which has the same magnitude as the statistical strain from the experimental results (Ding et al., 2019). It indicates the accuracy of the strain field obtained by the fractal function compared with the experimental results (Figure 4(a), 4(b)). The statistical lattice strain is 0.81% from Fig. 3. Figure 4(c) show the XRD patterns of as-cast CrFeCoNi HEA from the previous experiment (Tan et al., 2021). The averaged lattice strain is calculated by the following equation (Singh et al., 2006):

$$FWHM^2 \cos^2 \theta = \left(\frac{\lambda}{d} \right)^2 + \sigma^2 \sin^2 \theta \quad (6)$$

where FWHM is the full-width at half-maximum of the diffraction peak on the 2θ -scale, d is the grain size, σ is the lattice strain, and θ is the diffraction angle. The corresponding lattice strain is 0.72% from Figure 4(c) which is consistent with 0.81% from our experiment.

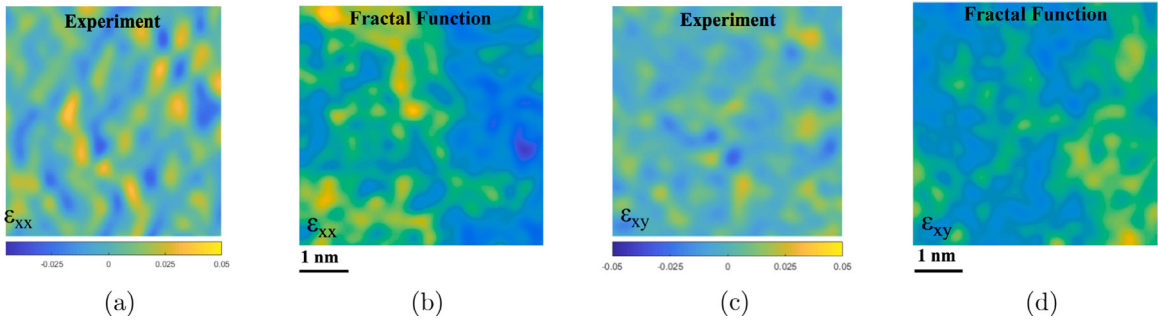


Fig. 3. The contour map of the normal residual strain and shear residual strain, which are obtained by the experiment and by the fractal function.

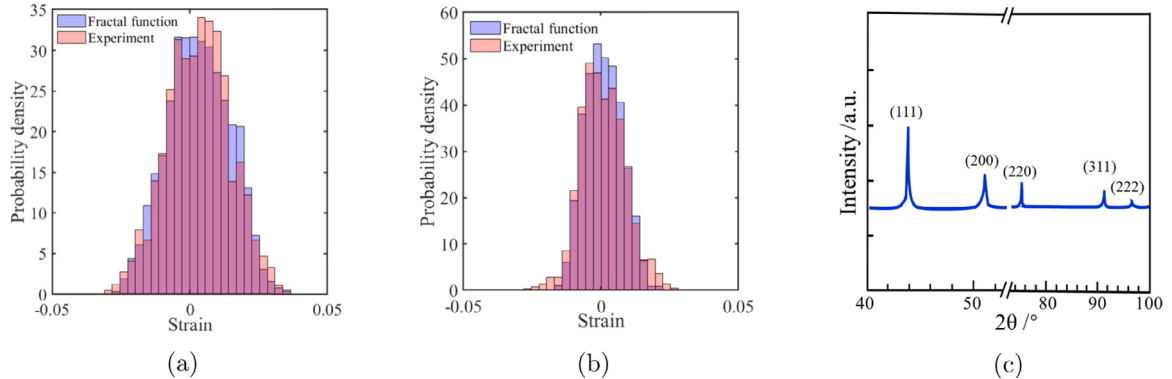


Fig. 4. The statistical distributions of the normal residual strain (a) and shear residual strain (b), which are obtained by the experiment and by the fractal function. XRD patterns of as-cast CrFeCoNi HEA (Tan et al., 2021) (c).

Table 1
The fractal dimension and strain amplitude for the strain components of the FeCoCrNi HEAs.

| Strain components, ϵ_{ij} | ϵ_{xx} | ϵ_{yy} | ϵ_{zz} | ϵ_{xy} | ϵ_{xz} | ϵ_{yz} |
|---|-----------------|-----------------|-----------------|-----------------|-----------------|-----------------|
| Fractal dimension, D_{ij} | D_{xx} | D_{yy} | D_{zz} | D_{xy} | D_{xz} | D_{yz} |
| | 3.8228 | 3.8228 | 3.8228 | 3.7911 | 3.7911 | 3.7911 |
| Strain amplitude, $H_{ij} (\times 10^{-4})$ | H_{xx} | H_{yy} | H_{zz} | H_{xy} | H_{xz} | H_{yz} |
| | 17.4528 | 17.4528 | 17.4528 | 9.2062 | 9.2062 | 9.2062 |

3. Computational methods

3.1. MD simulation

The dislocation mobility of the FeCoCrNi HEA is obtained by MD simulations. The relationship between the speed of dislocation movement and the shear stress can be well described by an empirical function at a specified temperature (Cho et al., 2017):

$$b\tau = \begin{cases} B(T)v & v \leq v_0 \\ B(T)v + D(v - v_0)^\alpha & v > v_0 \end{cases} \quad (7)$$

where $b = 0.253$ nm is the magnitude of the Burgers vector (Wang et al., 2018a), τ is the applied shear stress, $B(T)$ is the temperature-dependent linear drag coefficient, v_0 is the critical velocity from the linear regime to the nonlinear regime, D is the nonlinear drag coefficient, and α is a power law exponent for the nonlinear drag regime. Here, the linear drag coefficient is equal to 8.149×10^{-5} Pa s at 300 K from MD simulations (Figure 5(a)).

For the dislocation velocity $v \leq v_0$, the velocity of a dislocation is considered to be linearly related to the shear stress. When the dislocation velocity $v > v_0$, a nonlinear damping term is introduced, due to the damping effect from the emission of the ultrasonic wave. In the present work, the critical velocity occurs at a stress of 629 MPa, with a value of 1674 m/s. The statistic moving dislocation node velocity of the unirradiated sample in DDD simulation is presented (Figures 5(c), 5(d)). For DDD simulation without the strain field, the dislocation node velocity is much less than the critical velocity (Figure 5(c)). For the DDD simulation with the lattice strain, the dislocation node velocity is almost all less than the critical velocity (Figure 5(d)). Since the true dislocation velocity

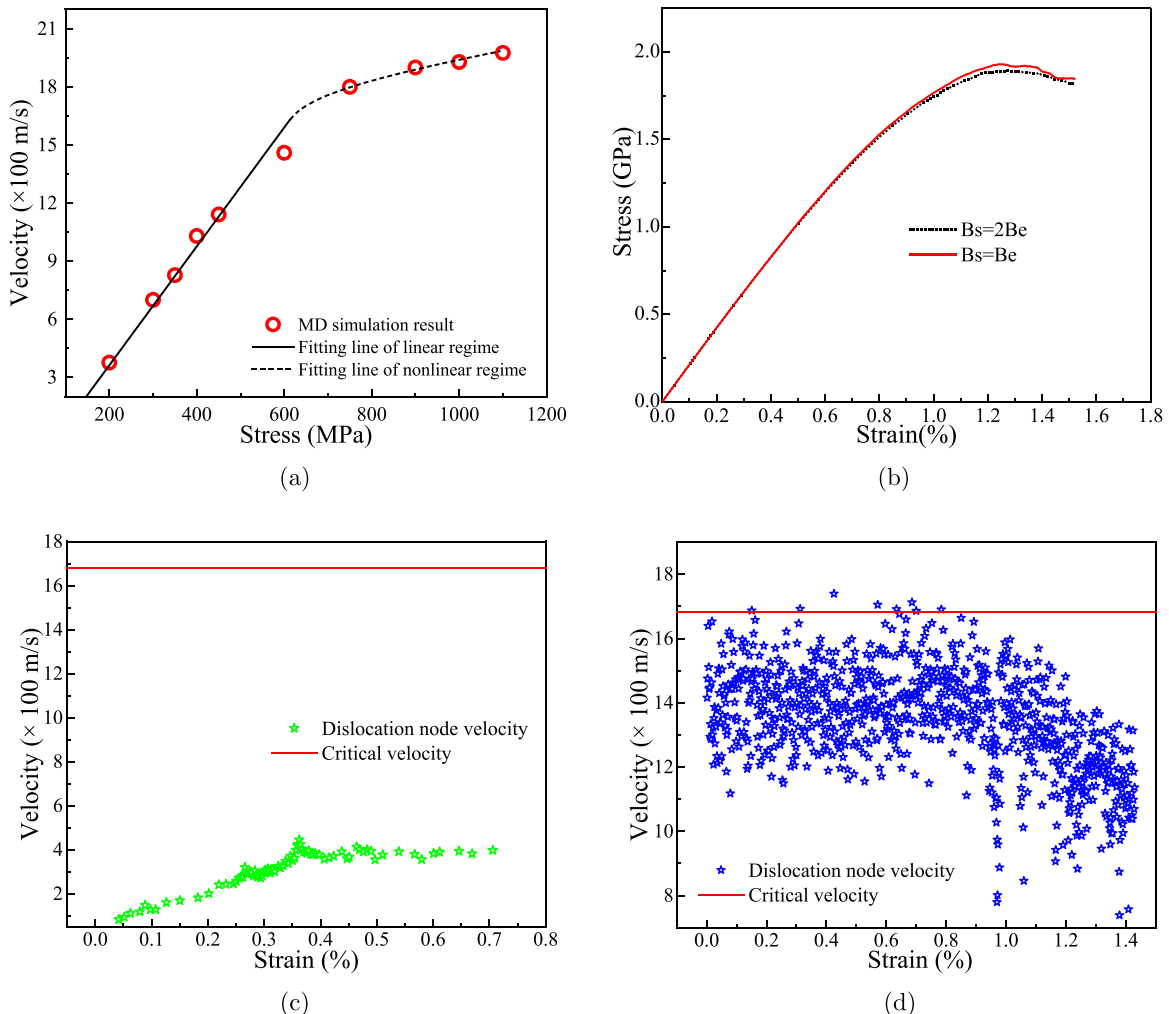


Fig. 5. (a) Dislocation velocity as a function of the applied shear stress for an edge dislocation in the FeCoCrNi HEA at room temperature using MD simulation. (b) The stress–strain curves for different drag coefficients. (c) The relationship between the statistic dislocation node velocity and strain without the heterogeneous lattice strain. (d) The relationship between the statistic dislocation node velocity and strain with the heterogeneous lattice strain.

includes the velocity contribution of two nodes, the dislocation velocity is usually smaller than the node velocity. In addition, the dislocation velocity in the irradiated samples is smaller because the dislocation loops pin the dislocations. Therefore, the dislocation velocity for the DDD simulation is considered to be in the linear drag regimes.

Before performing DDD simulations, we investigate the effects of the edge/screw dislocation mobility on the stress–strain curves of the FeCoCrNi HEA along the [001] direction. According to the result of Figure 5(b), the stress–strain curves obtained by DDD simulations are almost the same for different mobilities from the screw/edge dislocations. Consequently, different mobility values of screw/edge dislocations have few changes in the stress–strain curves of HEAs using DDD simulations (Chandra et al., 2018). Besides, recent MD simulations related to the dislocation mobility has proved that the drag coefficient of the screw dislocation shows no noteworthy difference with that of the edge dislocation in the FeNiCrCoCu HEA (Shen and Spearot, 2021). Therefore, the screw dislocation is considered to have the same mobility as the edge dislocation, agreeing with other recent DDD simulations (Lu et al., 2019; Rao et al., 2019; Sills et al., 2018).

Stacking fault introduced by mechanical deformation is one of the most important crystal defects, and in turn, plays a key role in the plastic deformation behavior of face-centered cubic (FCC) alloys (An et al., 2019). Here, stacking fault energy (SFE) generally affects the splitting of the dislocations, which should be pushed back together and then crosses slip (Gallagher, 1970). The cross slip becomes more difficult at the large split in the dislocations (An et al., 2019; Shih et al., 2021). The SFEs of 316L austenitic stainless, Cantor alloys, and FeCoCrNi HEA are 9.8, -46.2, and -42.2 mJ/m², respectively (Fig. 6). The values of SFE for the Cantor alloys and FeCoCrNi HEA are negative, and it is found to be in a good agreement with experimental data (Pei et al., 2021). Thus, the cross slip in the FeCoCrNi HEA happens easily compared with Cantor alloys, and this trend becomes more difficult than 316 L austenitic stainless (An et al., 2019; Shih et al., 2021). Recently, the difficulty in dislocation glide leads to massive cross-slip, for enhancing

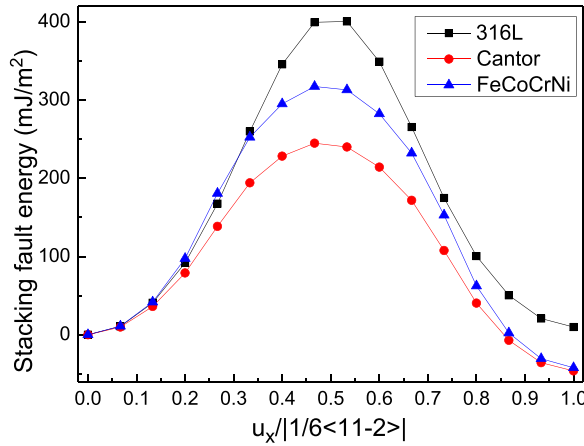


Fig. 6. The generalized stacking fault energy of 316L, Cantor alloys, and FeCoCrNi HEA.

the strength in AlCoCrFeNi HEA (Wang et al., 2018b). The extensive cross-slip is produced irregular dislocation cells deformed in carbon-containing FeCoCrNiMn HEA, and acts as the main deformation mechanism (Li et al., 2018). Thus, the cross-slip would occur in FeCoCrNi HEA at the extreme service environment.

3.2. DDD simulations

Based on the experimentally observed radiation defects, the radiation hardening of conventional alloys has been extensively studied using the DDD simulations (Arsenlis et al., 2012; Cui et al., 2018a,b, 2021). In traditional FCC alloys, the lattice friction stress is ignored due to its usually small value in DDD simulation (Sills et al., 2018; Rao et al., 2019). Previous results indicate that lattice friction stress is scaled linearly with the lattice distortion in HEAs (Zhao et al. (2019)). To qualitatively study the effect of lattice distortion on irradiation hardening behavior of HEAs by counting the large scale dislocation movement information. Hence, the blocking effect of heterogeneous lattice strain on dislocation movement is considered in the DDD simulation and the lattice friction stress is ignored.

To explore the effect of the extraordinary interaction of dislocations and radiation defects on radiation hardening, a DDD simulation method that considers the severe atomic lattice distortion in the irradiated FeCoCrNi HEAs needs to be developed. However, the classical Eshelby mean field theory, which is widely used in the traditional alloys, has the limitation in the DDD simulation for application of HEAs. Here, based on the random field theory (Li et al., 2022), the experimentally measured strain field of the FeCoCrNi HEA is embedded into the DDD simulation using the 3D fractal function. Therefore, a series of DDD simulations are implemented by embedding experimentally measured lattice strain field of the FeCoCrNi HEA, to investigate the role of heterogeneous lattice strain on radiation hardening at the mesoscopic scale.

The dislocation lines in the DDD simulation are constituted by a series of nodes and segments. The displacement of the dislocation is obtained by the moving speed of the integrating node. The movement of the dislocation node meets the dislocation mobility obtained from the MD simulation (Eq. (7)). The force, F_i , on the node i is obtained by accumulating the contributions of all segments connecting node, i :

$$F_i = \sum_j f_{ij} \quad (8)$$

where the force, f_{ij} , acting on the dislocation segment, ij , is obtained by a line integral of the Peach–Koehler force:

$$f_{ij} = \int_{C_j} N_i^j(s) f_{ij}^{PK}(s) dL(s) \quad (9)$$

where C_j represents the segment, ij . The shape function, $N_i^j(s)$, reflects the contribution of the Peach–Koehler force, $f_{ij}^{PK}(s)$, at the location of, s , for node, i

$$N_i^j(s) = s(0 \leq s \leq 1) \quad (10)$$

Here, $s = 0$ represents the location at the node, j , $s = 0.5$ locates in the midpoint of the dislocation segment, ij , and $s = 1$ shows the location at the node, i . The $f_{ij}^{PK}(s)$ depends on the local stress, $\sigma(s)$, on the segment acting on the dislocation segment, ij , which is composed of the load stress $\sigma^{ext}(s)$, the stress $\sigma^{disl}(s)$ from other dislocations, and the stress $\sigma^{HEA}(s)$ from the lattice distortion in the HEAs:

$$f_{ij}^{PK}(s) = [\sigma^{ext}(s) + \sigma^{disl}(s) + \sigma^{HEA}(s)] \cdot \mathbf{b}_{ij} \times \mathbf{t}_{ij} \quad (11)$$

Table 2
The material parameters of the FeCoCrNi HEA used in DDD simulations.

| Parameter | Symbol | Value |
|---------------------------------|--------|---------------------------------|
| Magnitude of the Burgers vector | b | 0.253 nm (Wang et al., 2018a) |
| Shear modulus | G | 86 GPa (Laplanche et al., 2018) |
| Poisson's ratio | ν | 0.2442 (Laplanche et al., 2018) |
| Dislocation core width | r_0 | 0.253 nm |

Table 3
The variation of radiation defect at different damage level of the radiated FeCoCrNi HEA (He et al., 2016).

| Damage level (dpa) | 0.036 | 0.102 | 0.170 | 0.511 |
|---|-------|-------|--------|--------|
| Loop mean radius (nm) | 5.175 | 9.716 | 14.555 | 31.213 |
| Loop number density (10^{21} num m $^{-3}$) | 5.500 | 5.812 | 6.170 | 6.258 |

Table 4
The relationship between the orientation of dislocation loop edge and habit plane for Frank loop configurations in the radiated FeCoCrNi HEA (He et al., 2016).

| Habit plane | Edge orientation | Burgers vector |
|-------------|------------------------|----------------|
| (111) | [10̄1], [01̄1], [1̄10] | [111]/3 |
| (11̄1) | [101], [011], [1̄10] | [11̄1]/3 |
| (1̄11) | [1̄01], [011], [110] | [1̄11]/3 |
| (1̄1̄1) | [101], [01̄1], [110] | [1̄11]/3 |

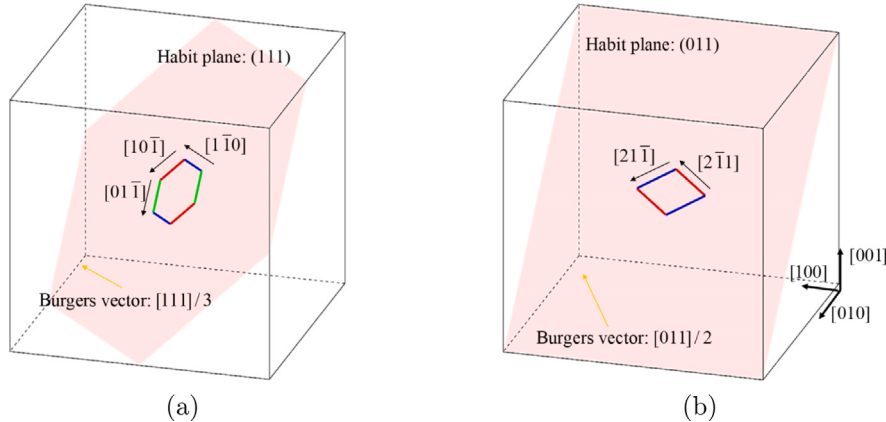


Fig. 7. The spatial configuration of Frank loop with (111) habit plane and rhombus perfect loop with (011) habit plane for the radiated FeCoCrNi HEA.

where $\sigma^{ext}(s)$ and $\sigma^{disl}(s)$ are calculated by the ParaDiS program. The stress, $\sigma^{HEA}(s)$, caused by the lattice distortion in the HEAs is obtained by the fractal function (Eq. (2)). t_{ij} is the unit vector parallel to the segment, ij , and b_{ij} is Burgers vector.

The irradiation defect types, spatial structure, sizes and densities of the FeCoCrNi HEA have been observed in detail by the corresponding experiments (He et al., 2016). The Frank loops with $b = \langle 111 \rangle/3$ and rhombus perfect loops with $b = \langle 110 \rangle/2$ are observed in FeCoCrNi HEA at 1250 kV under a temperature of 400 °C (He et al., 2016). The major axis of the elliptical Frank loops along ⟨110⟩ directions, and the aspect ratio with time measured is equal to 1 at the irradiation time of 30 min (He et al. (2016)). The loop diameter and number density for various irradiation doses are listed in Table 3.

Based on the above detailed experimental characterization of the radiation defect structure, a series of DDD simulation models are constructed. The size of a cube simulation box is about 0.75 μm, and the periodic-boundary condition is used in all six surfaces for studying the irradiation hardening behavior using the classic DDD simulation (Lehtinen et al., 2018). The number of dislocation loop is obtained according to the number density of experimental observations and the size of simulation (Fig. 3). The number ratio of the Frank loop and rhombus perfect loop is close to 3:1 (He et al., 2016). These loops are randomly positioned within the simulation box. For Frank loop, hexagonal loops with edges along ⟨110⟩ directions, {111} habit plane, and Burgers vector of $b = \langle 111 \rangle/3$ are considered (Arsenlis et al., 2012; He et al., 2016). For the rhombus perfect loop, two edges are along [21̄1] and [2̄11] with the {110} habit plane. The correspondence between the orientation of edge and habit plane is listed in Tables 4 and 5. The spatial configuration of Frank loop with (111) habit plane and rhombus perfect loop with (110) habit plane is presented in Fig. 7. The number of dislocation loops on each habit plane is evenly distributed.

All DDD simulations implemented in the current work are applied using ParaDiS, which is an open-source code developed by the Lawrence Livermore National Laboratory (Bulatov et al., 2006). The material parameters at room temperature used in DDD

Table 5

The relationship between the orientation of dislocation loop edge and habit plane for rhombus perfect loop configurations in the radiated FeCoCrNi HEA (He et al., 2016).

| Habit plane | Edge orientation | Burgers vector |
|-------------|------------------|----------------|
| (011) | [2̄1̄1], [21̄1] | [011]/2 |
| (01̄1) | [2̄11̄], [211] | [01̄1]/2 |
| (10̄1) | [12̄1], [121] | [10̄1]/2 |
| (101) | [12̄1̄], [1̄21] | [101]/2 |
| (̄110) | [11̄2], [112] | [̄110]/2 |
| (110) | [1̄12], [1̄12] | [110]/2 |

simulations of the FeCoCrNi HEA are listed in [Table 2](#). The initial dislocation configuration is consisted of 12 straight dislocations in the $1/2\langle 110 \rangle$ slip system corresponding to an initial density of $2.5 \times 10^{13} \text{ m}^{-2}$. This sample is firstly relaxed to an equilibrium state, and subjected to the constant strain rate of $1 \times 10^6 \text{ s}^{-1}$ along [001] (Lehtinen et al., 2018). The Frank loops are the strong obstacles for the unpinning reactions involving the Orowan process (Rodney, 2004). Here, the computational cost would be reduced by representing Frank loops without the stacking faults, and each Frank loop is constructed by six straight dislocation segments (Cui et al., 2017). So that, the elastic stress field of the Frank loop is accurately obtained (Cui et al., 2017).

4. Results

4.1. Irradiation hardening

[Fig. 8](#) shows the relationship between the yield strength and the dislocation loop characteristic at different irradiation doses from the previous experiment (He et al., 2016). As can be seen from [Fig. 3](#), the increase of the irradiation dose mainly leads to the increase of the dislocation loop size in the FeCoCrNi HEA, and the change in the dislocation density is negligible. Therefore, in the following discussion, we would directly explore the influence of the dislocation-loop size on the radiation hardening behavior. [Figure 8\(a\)](#) shows the stress-strain curve for dislocation loop with different sizes. The mechanical behavior in the dislocation loop free HEA is firstly an initial elastic stage followed by the yielding, and then work hardening at a constant rate. When the loops are existence in the radiated HEA, the flow stress decreases after the yield point (Arsenlis et al., 2012), and the trend of the stress drop is more pronounced as the dislocation loop radius increases ([Figure 8\(a\)](#)). The irradiation induced dislocation loop strengthening in the traditional metals can be described by a well-established dispersed barrier-hardening (DBH) model (Kumar et al., 2016; Peng et al., 2022).

$$\Delta\sigma_y = \alpha M G b (ND)^{1/2} \quad (12)$$

where M is the Taylor factor, which is 3.06 for the FCC structured HEA (Fang et al., 2019), α is a constant for the average barrier strength of dislocation loops, assumed as 0.4 (for strong obstacles such as dislocation loops) (Kumar et al., 2016), G is the shear modulus, b is the Burgers vector ([Fig. 2](#)), D is the loop diameter, and N is the loop number density ([Fig. 3](#)). [Figure 8\(b\)](#) shows a good linear correlation between the DDD result and DBH model. It demonstrates that the DDD simulation can capture a typical irradiation strengthening in the conventional alloys (Kumar et al., 2016).

To investigate the effect of unusual dislocation motions induced by the heterogeneous lattice strain on radiation hardening at the mesoscopic scale, a series of DDD simulations are implemented by embedding experimentally measured FeCoCrNi HEA lattice strains, according to the random field theory (Li et al., 2022). In order to avoid the randomness related to the initially built model generated by the DDD simulation, three independent samples with the same average loop size/density are considered ([Figure 9\(a\)](#)). The degree of the stress drop is almost unchanged for the dislocation loops with different radii, indicating the insensitivity of radiation hardening to defect size in the radiated HEA with severe lattice distortion. The peak of the heterogeneous lattice strain hinders the dislocation movement to improve the critical resolved shear stress (CRSS) at the plastic deformation stage, resulting in the dislocations to cut through dislocation loops more easily. To clearly investigate the microstructural evolution, the first group of the tensile samples are selected. The statistical stress increment shows the lower irradiation hardening in the HEAs ([Figure 9\(b\)](#)), in consistent with the experimental observations (El-Atwani et al., 2019; Jin et al., 2016; Li et al., 2019a, 2021b; Sadeghilaridjani et al., 2020; Zhang et al., 2021).

4.2. Lattice distortion-controlled irradiation defect evolution

In order to explore the influence of the dislocation dynamic evolution on the irradiation hardening during the tensile deformation, the snapshots of dislocation structures illustrated by the slip plane for the FeCoCrNi HEA without and with heterogeneous lattice strain are presented in [Figs. 10](#) and [11](#), respectively. Moreover, to quantitatively describe the cross-slip, the increased dislocation density from the cross-slip is counted in [Fig. 12](#). The generation of few cross-slip results in an insignificant increase in the dislocation density for the sample with small size dislocation loops at the dose of 0.036 dpa without lattice distortion ([Figs. 10](#) and [12](#)). A small number of the jogs is generated by the interactions between the dislocation-dislocation loops. The size of the dislocation loop increases with the increasing irradiation dose (He et al., 2016), and thus the cross-slip occurs frequently to cause a large dislocation

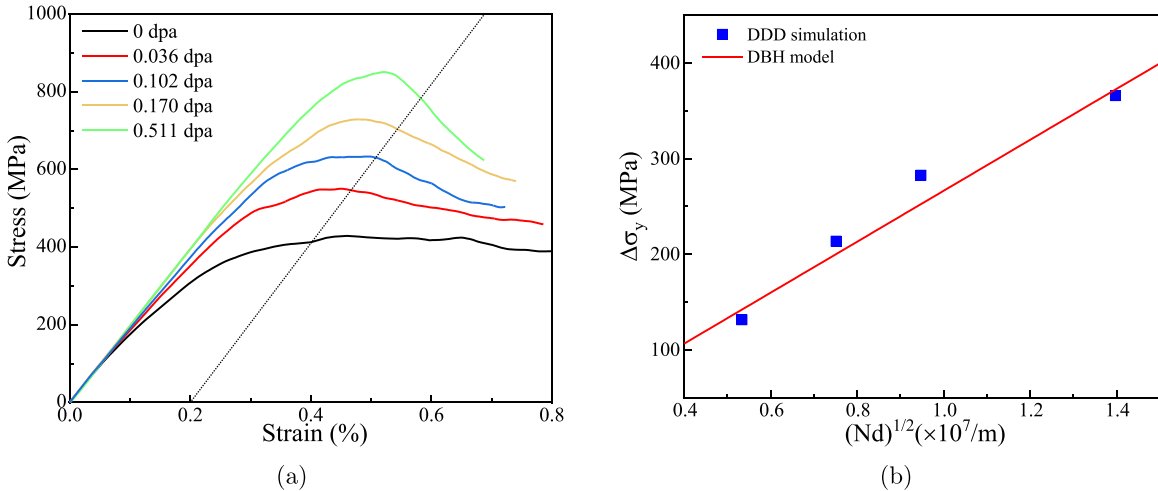


Fig. 8. (a) The stress–strain curve of the FeCoCrNi HEA without the local lattice distortion. (b) The correlation between the strengthening increment from irradiation defects and the square root of the product of defect density and size.

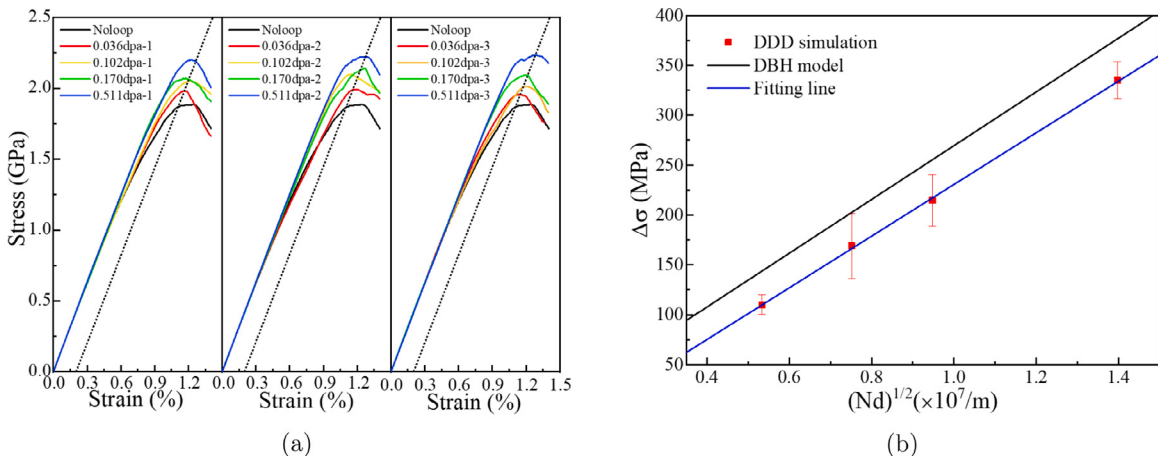


Fig. 9. (a) The stress–strain curves of the FeCoCrNi HEA without local lattice distortion. (b) Correlation between the irradiation hardening and the square root of the product of defect density and size. The stress increment is counted by three independent samples.

density (Fig. 10). On the one hand, the increase of the dislocation loop size improves the probability for the interaction between dislocations and dislocation loops. On the other hand, the interactions between the large-sized dislocation loops and dislocations form the superjogs (Fig. 10), which are not easy to be dragged and annihilated (Agrawal et al., 2022; Cui et al., 2017).

In the strain field induced by the heterogeneous lattice distortion, the driving force for the dislocation motions from the other slip planes is greater than that from the main slip plane, thus increasing the frequency of the cross-slip (Ding et al., 2019; Li et al., 2022). Therefore, unlike conventional alloys, the low probability for the spatial interaction of dislocation and dislocation loop would produce a large amount of the cross-slip in HEAs (Fig. 11). Compared to the sample without the heterogeneous lattice strain (Fig. 10), the probability of cross-slip is greater in the FeCoCrNi HEA with the lattice distortion (Figs. 11 and 12).

The value of Schmid factor for the dislocations with Burgers vectors of $[110]/2$ and $[\bar{1}10]/2$ is zero for the [001] tensile direction in the FCC crystal. It shows that these dislocations are not activated. The dislocations on the remaining slip systems have some values of Schmid factor (about 0.4082), indicating that the dislocations of these slip systems are activated. Therefore, the immovable dislocations here include the dislocations with Burgers vectors of $[110]/2$ and $[\bar{1}10]/2$, and the dislocation junctions on the non-slip planes generated by dislocation interactions that do not belong to the 12 slip systems (Sills et al., 2018). The statistical analysis of the movable and immovable dislocation densities with the increasing strain shows that massive dislocation proliferation occurs in FeCoCrNi HEAs with a lattice distortion (Fig. 13). The dislocation density increases faster as the strain increases for the larger-radius dislocation loop, which corresponds to the results of Figs. 10 and 11. Interestingly, in the FeCoCrNi without a heterogeneous lattice strain, the densities of the immovable dislocations exceed those of the movable dislocations with the increasing strain (Figure 13(a)), whereas the opposite tend is observed in the sample with a heterogeneous lattice strain (Figure 13(b)).

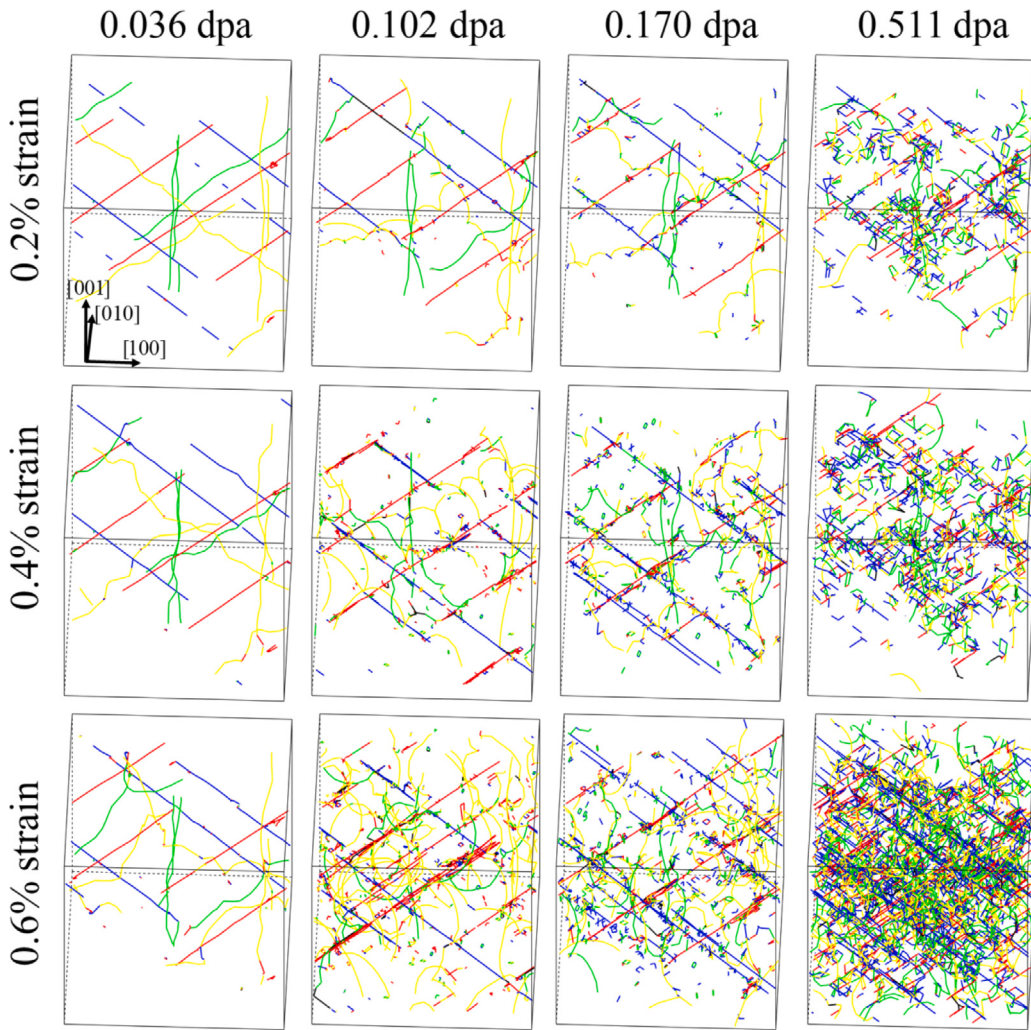


Fig. 10. Dislocation structures at the strains of 0.2, 0.4, and 0.6% for different irradiation doses in the FeCoCrNi HEA without local lattice distortion. Dislocations are colored on slip planes. The dislocations on the slip plane (— blue line), slip plane (— red line), slip plane (— light-yellow line), and slip plane (— green line). (For interpretation of the references to color in this figure legend, the reader is referred to the web version of this article.)

In order to investigate the lattice distortion effect on the irradiation defect annihilation in the FeCoCrNi alloy, Fig. 14 shows the variation of the numbers of annihilated dislocation loops with the increasing strain. In the elastic strain stage, the number of the annihilated dislocation loops in the FeCoCrNi alloy with lattice distortion is less than that in the FeCoCrNi alloy without lattice distortion (Figure 14(a)), because lattice strain pins the dislocations and prevents the encounter between dislocation and dislocation (Ding et al., 2019; Li et al., 2022). The heterogeneous lattice strain obstructs the dislocation movement and makes the yield strain move backward. Therefore, when the yield point is crossed into the plastic deformation stage, the dislocation density proliferates explosively to promote the increase of the dislocation loop annihilation rate (Figure 14(b)), which is consistent with the evolution law of dislocation configuration in FeCoCrNi alloys with lattice distortion (Fig. 11). For dislocation loops of all sizes, the annihilation rate of the Frank loop is higher than that of the rhombus perfect loop (Fig. 14), possibly due to the different dislocation line energies caused by the unequal magnitude of Burgers vectors between the Frank loop and rhombus perfect loop.

5. Discussion

5.1. Irradiation defect and dislocation interaction

To deeply understand the complex dislocation evolution, the movement characteristics of a single dislocation should be revealed in the irradiated HEAs. The interaction of the single dislocation with the Frank loop and rhombus perfect loop is investigated in detail based on the DDD simulations (Fig. 15). For the Frank loop, the first case considers the interaction of one $1/31\bar{1}\bar{1}$ loop

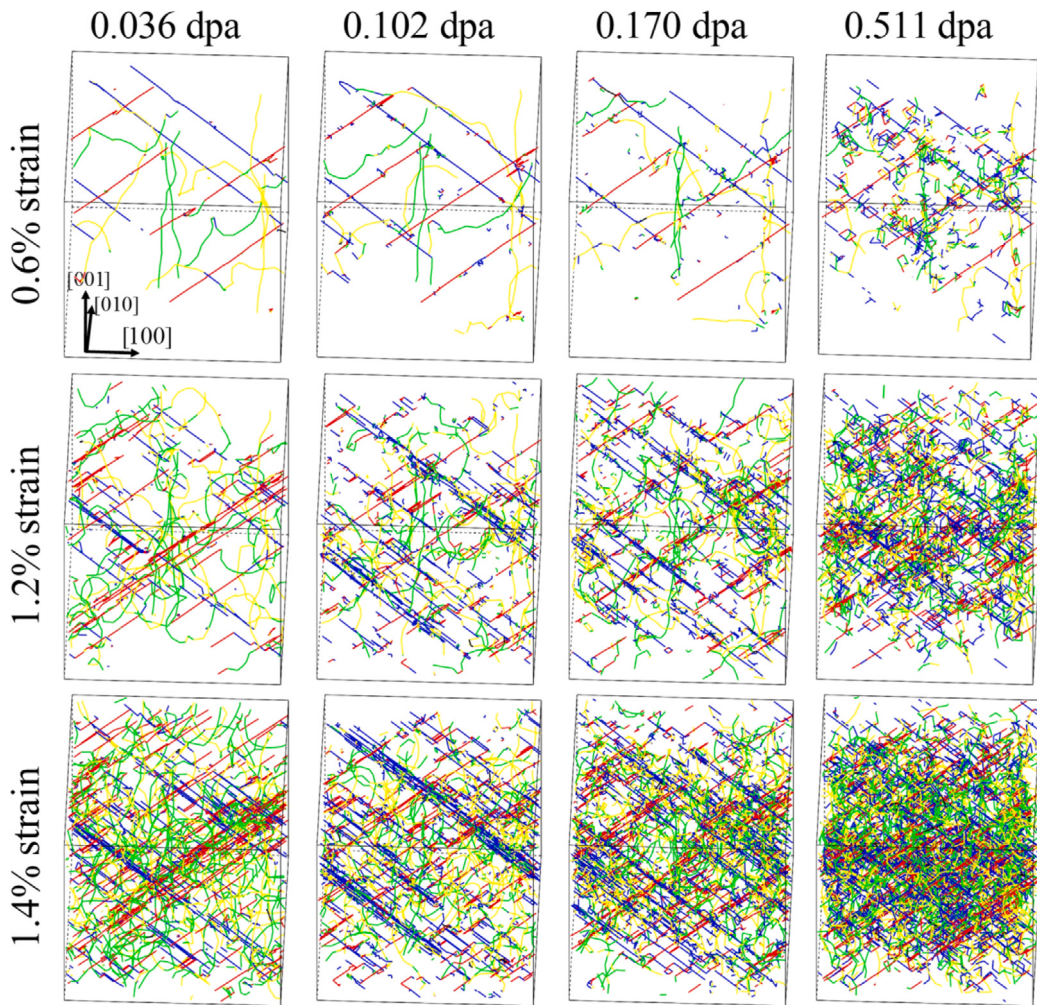


Fig. 11. Dislocation structure at the strains of 0.6, 1.2, and 1.4% for different irradiation doses in FeCoCrNi HEA with local lattice distortion. Dislocations are colored on slip planes. The dislocations on the slip plane (— blue line), slip plane (— red line), slip plane (— light-yellow line), and slip plane (— green line). (For interpretation of the references to color in this figure legend, the reader is referred to the web version of this article.)

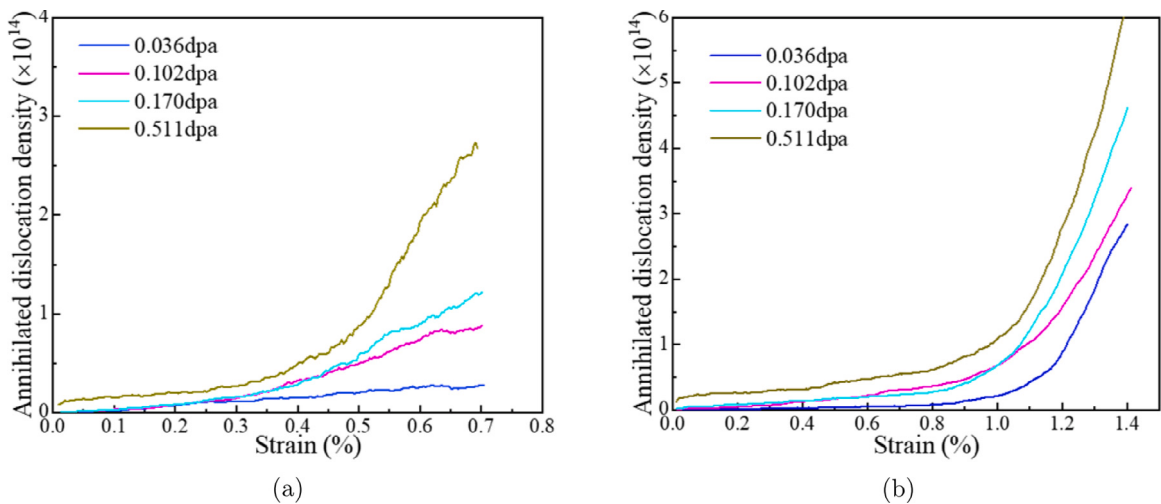


Fig. 12. The increased dislocation density from cross-slip for different irradiation doses in FeCoCrNi HEA without local lattice distortion (a) and with local lattice distortion (b).

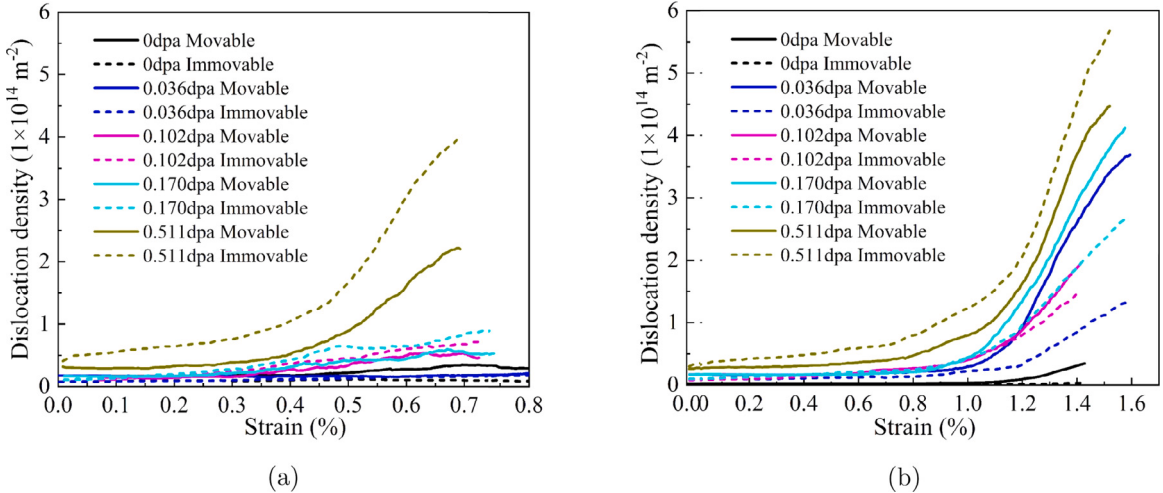


Fig. 13. Density evolution diagram of movable and immovable dislocations in the FeCoCrNi HEA without (a) and with (b) local lattice distortion.

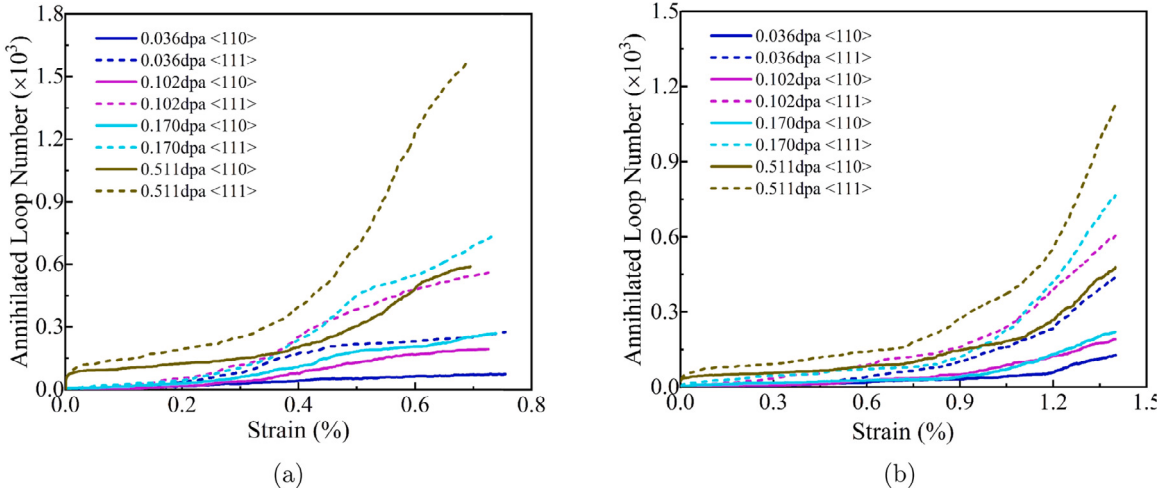


Fig. 14. Number of loops annihilated by dislocations vs. strain in the FeCoCrNi HEA without local lattice distortion (a) and with local lattice distortion (b).

and one $1/2[011](1\bar{1}\bar{1})$ dislocation with the same slip plane. Similar to previous work (Lee et al., 2001), a synchro-shear process is observed in the interaction of $1/2[011](1\bar{1}\bar{1})$ dislocation with a $1/31\bar{1}\bar{1}$ Frank dislocation loop (Figure 15a), resulting in the faulted loop with a high index Burgers vector of $b = 1/6[21\bar{5}]$:

$$\frac{1}{2}[011] + \frac{1}{3}[1\bar{1}1] = \frac{1}{6}[21\bar{5}] \quad (13)$$

Due to the formation of the $b = 1/6[21\bar{5}]$ -type high index loops would require a high energy in shifting the $1/3[1\bar{1}\bar{1}]$ -type loop by $1/2[011]$ -type dislocation, such an interaction contributes to the strong strain hardening in the FeCoCrNi HEA. The different slip planes between the dislocation and loop are considered in the second case (Figure 15b). When a dislocation is close to the dislocation loop, the dislocation is attracted and then pinned. Then, a dislocation junction is observed from the interaction between the $1/2[011](1\bar{1}\bar{1})$ dislocation and $1/31\bar{1}\bar{1}$ Frank loop. Two new dislocation segments with Burgers vector of $1/6[2\bar{1}\bar{1}]$ are generated by:

$$\frac{1}{2}[0\bar{1}\bar{1}] + \frac{1}{3}[111] = \frac{1}{6}[2\bar{1}\bar{1}] \quad (14)$$

As the shear stress increases, the dislocation continuously moves forward, to cut through dislocation loop. This process results in that the original large size dislocation loops become several small dislocation loops after being cut by dislocations. The dislocation loop is cut by the dislocation several times and then annihilated (Figure 15b). Due to the formation of the $b = 1/6 [21\bar{5}]$ -type high index loops would require a high energy in shifting the $1/3[1\bar{1}\bar{1}]$ -type loop by $1/2 [011]$ -type dislocation, such an interaction

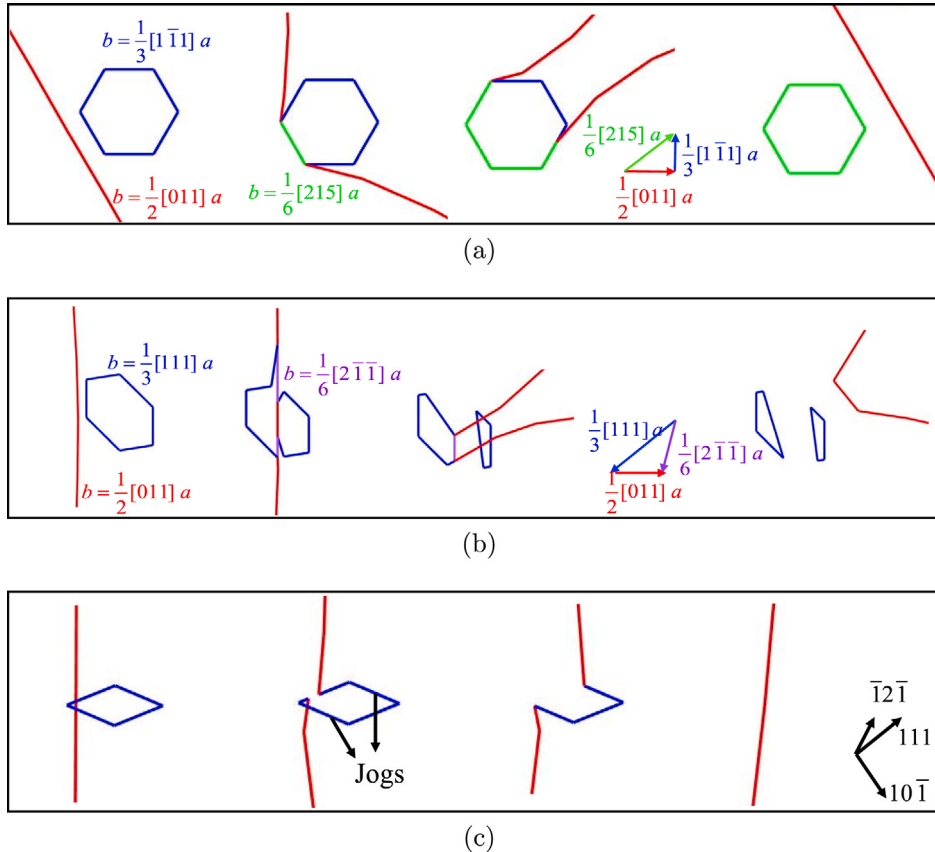


Fig. 15. (a) The dislocation with Burgers vector of $1/2[011]$ and slip plane of $(1\bar{1}1)$ interacts with Frank loop with Burgers vector of $1/3[1\bar{1}1]$ and habit plane of $(1\bar{1}1)$. Here, dislocation is coplanar with the dislocation loop. (b) The dislocation with Burgers vector of $1/2[011]$ and slip plane of $(1\bar{1}1)$ interacts with Frank loop with Burgers vector of $1/3[111]$ and habit plane of (111) . Here, the dislocation slip plane and dislocation loop are not coplanar. (c) The dislocation with Burgers vector of $1/2[10\bar{1}]$ and slip plane of (111) interacts with rhombus perfect loop with Burgers vector of $1/2[10\bar{1}]$ and habit plane of $(10\bar{1})$. Here, the dislocation slip plane and dislocation loop are not coplanar. Since there is no coplanar case between the dislocation with slip plane of $\{111\}$ and rhombus perfect dislocation loop with habit plane $\{110\}$, only the evolution process of the intersection of dislocation and dislocation loop is shown in (c).

contributes to the strain hardening in the FeCoCrNi HEA. The $1/2[10\bar{1}](111)$ dislocation passes through the edge and center of the rhombus perfect loop (Figure 15c). When the dislocation touches the edge of a loop, a jog pair forms spontaneously, similar to the previous DDD simulation (Gururaj et al., 2015). Therefore, the rhombus perfect dislocation loops in the FeCoCrNi alloy are absorbed in the form of jogs.

To explore the origin of cross-slip in the irradiated FeCoCrNi alloy, Fig. 16 shows the magnified views from DDD simulation under the irradiation dose of 0.170 dpa at different strains. In FeCoCrNi alloys without a severe lattice strain, the cross-slip generation is closely related to the reaction between dislocations and rhombus perfect dislocation loops. As presented in Figure 16(a), the rhombus perfect dislocation loop on the $(\bar{1}01)$ habit plane consists of dislocations in two slip systems of $1/2[\bar{1}01](111)$ and $1/2[10\bar{1}](1\bar{1}1)$, which are on different slip planes with the same Burgers vector (He et al., 2016). When the slip dislocation is close to the loop, the $1/2[\bar{1}01](111)$ slip dislocation reacts with a $1/2[10\bar{1}](1\bar{1}1)$ dislocation belonging to one side of the rhombic dislocation loop, leading to the formation of a collinear reaction (Sills et al., 2018). The $1/2[10\bar{1}](1\bar{1}1)$ dislocation on the other side of the rhombic dislocation loop becomes a jog. The $1/2[\bar{1}01](111)$ dislocation belonging to a loop continues to expand to form the cross-slip. The large-sized rhombic dislocation loop interacts with the dislocation to form a strong super-jog (Figure 16(a)), which is not easily annihilated (Agrawal et al., 2022; Cui et al., 2017). Hence, more superjogs promote a large number of the cross-slips, leading to an increase of the dislocation density (Fig. 10).

In the FeCoCrNi alloy with the severe lattice distortion, the cross-slip process is not only controlled by the dislocation and dislocation loop reactions, but also strongly depends upon a heterogeneous lattice strain (Figure 16(b)). The occurrence of the cross-slip event takes place in the position, where the stress acting on a secondary slip plane is high enough (Shao et al., 2019). Alternating strain peaks and valleys caused by a severely heterogeneous lattice distortion provide a large number of points, which greatly facilitate the occurrence of a cross-slip event (Fig. 11). Moreover, the cross-slip induced by heterogeneous lattice strain promotes the spatial extent of dislocation motion, leading to increase the probability of interaction between dislocations and irradiation-induced dislocation loops (Figure 16(b)). This process further facilitates the generation of the cross-slip. Due to the chain reaction, hence,

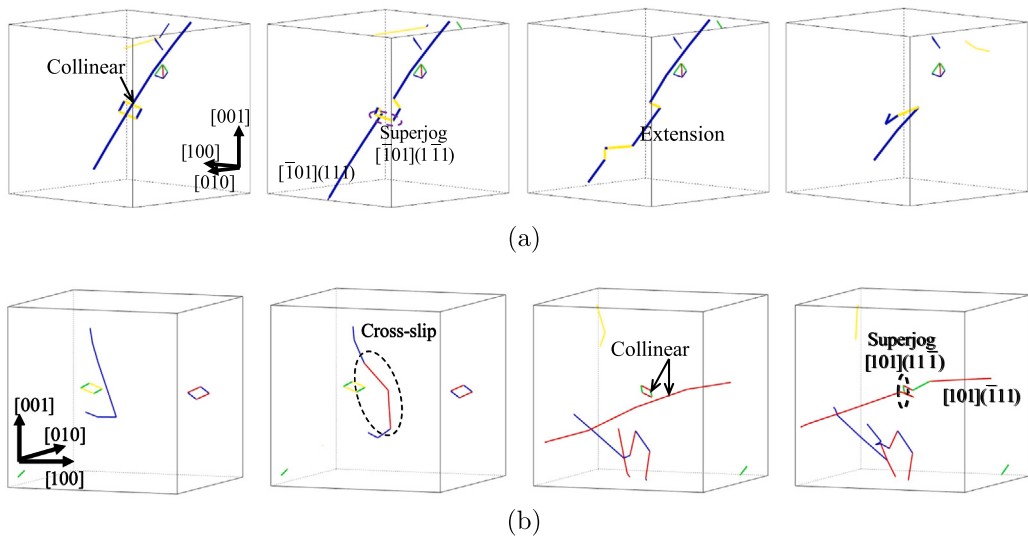


Fig. 16. The cross-slip process in the FeCoCrNi alloy without (a) and with (b) local lattice distortion. The dislocations on the slip plane (— blue line), slip plane (— red line), slip plane (— yellow line), and slip plane (— green line). (For interpretation of the references to color in this figure legend, the reader is referred to the web version of this article.)

heterogeneous lattice strain coupled with the dislocation–dislocation loop reaction greatly promotes the generation of cross-slip in the short period range.

5.2. Statistical analysis of irradiation defect

The strain localization has received considerable attention due to its significant control over the degradation of mechanical properties of irradiated alloys (Barton et al., 2013; Diaz de la Rubia et al., 2000; Erinosh and Dunne, 2015; Ghoniem et al., 2001; Li et al., 2019b; Po and Ghoniem, 2013) which is often attributed to the formation of the microscale local plastic regions called a ‘defect free channel’. Although these phenomena have been known in the conventional alloys, the potential physical mechanisms related to the severe lattice distortion have not clearly elucidated in HEAs. Here, the snapshots of the dislocation loop distribution in the deformed FeCoCrNi without and with local lattice distortion are presented in Fig. 17. The wider defect-free channels in the FeCoCrNi without local lattice distortion than that in the FeCoCrNi with local lattice distortion are observed, showing a lower local plastic flow capacity. The high lattice strain field induced by lattice distortion makes the dislocation move in a state of a high shear stress at the plastic deformation stage. In this state, the hindering effect of irradiation defects on dislocations is relatively weak, reducing the extended effect on the cross-slip (Ding et al., 2019; Li et al., 2022). Conversely, a large number of narrow defect-free channels occur in the FeCoCrNi HEA with a local lattice distortion (Fig. 17), which is consistent with the high density dislocation (Fig. 11). The high heterogeneous lattice strain provides a large amount of the pinning points conducive to the cross-slip. The spatial distribution of the cross-slip is relatively random, and then this trend promotes the generation of many defect-free dislocation channels. Therefore, a high heterogeneous lattice strain improves the localized plastic deformation in the irradiated HEAs.

The irradiation induced defects act as a strong obstacle to hinder dislocation slip, resulting in the inhomogeneous dislocation distributions from dislocation pileups (Das et al., 2020; Liu et al., 2022). In order to further quantify the effect of lattice distortion on the localized plastic deformation behavior, the spatial distribution of dislocation density is counted by taking a pixel map (Fig. 18). In the FeCoCrNi HEA without lattice distortion, a lot of the dislocation tangles appear in the same local area to form a concentrated distribution for the high dislocation density (Figure 18(a)). A cross-slip event occurs with the same probability everywhere, and then causes that the dislocation density is randomly distributed in the FeCoCrNi with the lattice distortion (Li et al., 2022), due to the spatial random distribution of the strain peaks/valleys (Figure 18(b) and 18(c)). The coefficient of variation is defined as the ratio of the standard deviation to the mean. It is adopted as a normalized measure of the dispersion degree for the density distribution in the dislocation and dislocation loop (Figure 18(d)). The coefficient of variation in the FeCoCrNi with lattice distortion is lower than that without lattice distortion. This observation indicates that the lattice distortion promotes a more uniform plastic deformation of the irradiated HEA. Hence, in the FeCoCrNi with lattice distortion, not only the dislocation density is high, but also its distribution is uniform. This trend suggests that the severe atomic lattice distortion effectively improves the irradiation performance in the HEA.

6. Conclusions

To summarize, the random field theory informed DDD simulations based on the results of HRTEM are developed, and used to investigate the irradiation hardening behavior of the FeCoCrNi HEAs. Compared to the traditional alloys, HEAs exhibit the low

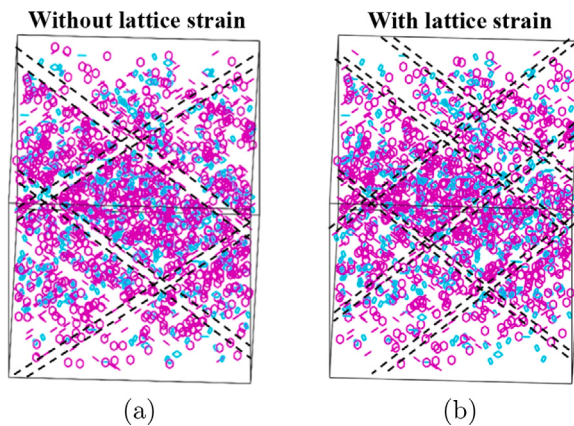


Fig. 17. The distribution of dislocation loops at the strains of 0.6% and 1.4% for an irradiation dose of 0.170 dpa in the FeCoCrNi HEA without (a) and with (b) local lattice distortion. The prismatic dislocation loop with $b = 1/2\langle 110 \rangle$ (Cyan line), and the Frank dislocation loop $b = 1/3\langle 111 \rangle$ (Magenta line). Two parallel black dotted lines indicate the defect-free channel. (For interpretation of the references to color in this figure legend, the reader is referred to the web version of this article.)

irradiation hardening due to the severe atomic lattice distortion. The complex interaction processes of dislocations with the hexagon Frank loop and rhombus perfect loop in the irradiated HEAs are studied at the micrometer scale. An unconventional dislocation mechanism of cross-slip between dislocations and rhombus perfect loops through the collinear reaction is observed for the first time. In the FeCoCrNi HEAs, the dislocation cross-slip originates from (i) the strong pinning points from the second slip plane; (ii) and the reaction of dislocations and rhombus perfect dislocation loops. In addition, a large number of the dislocation cross-slips generated from the deformation lead to the dense narrow defect free channels in the FeCoCrNi HEAs with heterogeneous lattice strain. Therefore, the spatial distribution of strain localization is relatively random, and then enhances the local plastic deformation to improve the radiation resistance of the HEAs.

CRediT authorship contribution statement

Yang Chen: Software, Methodology, Writing – original draft, Investigation, Methodology, Writing – review & editing. **Shuo Wang:** Software, Methodology, Writing – original draft, Investigation, Methodology, Writing – review & editing. **Hui Feng:** Software, Methodology, Validation, Writing – review & editing. **Weipeng Li:** Formal analysis, Investigation, Data curation, Visualization, Writing – review & editing. **Bin Liu:** Project administration, Investigation, Validation, Writing – review & editing. **Jia Li:** Conceptualization, Project administration, Investigation, Writing – original draft, Writing – review & editing. **Yong Liu:** Supervision, Conceptualization, Writing – review & editing. **Peter K. Liaw:** Supervision, Funding acquisition, Writing – review & editing. **Qihong Fang:** Supervision, Funding acquisition, Conceptualization, Writing – review & editing.

Declaration of competing interest

The authors declare that they have no known competing financial interests or personal relationships that could have appeared to influence the work reported in this paper.

Data availability

Data will be made available on request.

Acknowledgments

The authors would like to deeply appreciate the supports from National Natural Science Foundation of China (U2267252, 12172123, and 12072109), Natural Science Foundation of Hunan Province, China (2022JJ20001 and 2021JJ40032), The science and technology innovation Program of Hunan Province (2022RC1200), and Natural Science Foundation of Changsha City (kq2202139). PKL very much appreciates the support from the National Science Foundation, United States (DMR-1611180, 1809640, and 2226508).

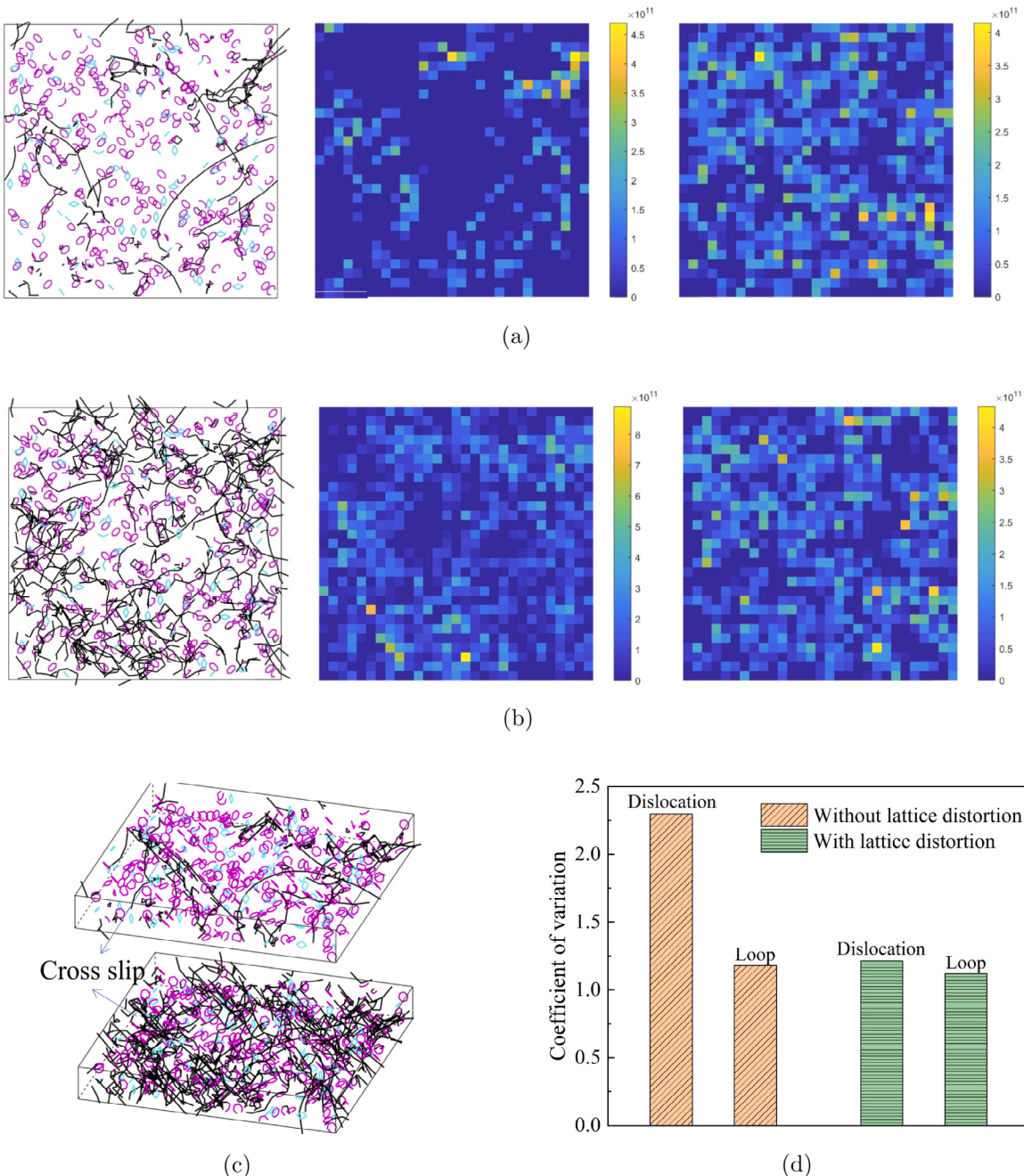


Fig. 18. The dislocation and dislocation loop configurations, and the pixel image of the density distribution for the dislocation and dislocation loop in the FeCoCrNi HEA without (a) and with (b) local lattice distortion, where the strains are 0.6% and 1.4%, and the irradiation dose is 0.170 dpa. Black line (—) is dislocation, the prismatic dislocation loop with $b = 1/2\langle 110 \rangle$ (— Cyanogen line), and the Frank dislocation loop $b = 1/3\langle 111 \rangle$ (— Magenta line). Each small color block in the pixel image represents the area of 25×25 nm, and the color of the block depends on the density. (c) The dislocation configuration from the other view. (d) The coefficient of variation for the dislocation density and dislocation loop density in the FeCoCrNi HEA without and with local lattice distortion. (For interpretation of the references to color in this figure legend, the reader is referred to the web version of this article.)

References

- Agrawal, P., Karthikeyan, S., Makineni, S.K., Gault, B., Banerjee, D., 2022. Dynamic strain aging in the intermediate temperature regime of near- α titanium alloy, IMI 834: Experimental and modeling. *Acta Mater.* 222, 117436.
- Aizenshtain, M., Ungarish, Z., Woller, K., Hayun, S., Short, M., 2020. Mechanical and microstructural response of the Al0.5CoCrFeNi high entropy alloy to Si and Ni ion irradiation. *Nucl. Mater. Energy* 25, 100813.

- An, X., Wu, S., Wang, Z., Zhang, Z., 2019. Significance of stacking fault energy in bulk nanostructured materials: Insights from Cu and its binary alloys as model systems. *Prog. Mater. Sci.* 101, 1–45.
- Arsenlis, A., Rhee, M., Hommes, G., Cook, R., Marian, J., 2012. A dislocation dynamics study of the transition from homogeneous to heterogeneous deformation in irradiated body-centered cubic iron. *Acta Mater.* 60 (9), 3748–3757.
- Ausloos, M., Berman, D., 1985. A multivariate Weierstrass–Mandelbrot function. *Proc. R. Soc. Lond. Ser. A Math. Phys. Eng. Sci.* 400 (1819), 331–350.
- Barr, C.M., Nathaniel II, J.E., Unocic, K.A., Liu, J., Zhang, Y., Wang, Y., Taheri, M.L., 2018. Exploring radiation induced segregation mechanisms at grain boundaries in equiatomic CoCrFeNiMn high entropy alloy under heavy ion irradiation. *Scr. Mater.* 156, 80–84.
- Barton, N.R., Arsenlis, A., Marian, J., 2013. A polycrystal plasticity model of strain localization in irradiated iron. *J. Mech. Phys. Solids* 61 (2), 341–351.
- Bulatov, V.V., Hsiung, L.L., Tang, M., Arsenlis, A., Bartelt, M.C., Cai, W., Florando, J.N., Hiratani, M., Rhee, M., Hommes, G., et al., 2006. Dislocation multi-junctions and strain hardening. *Nature* 440 (7088), 1174–1178.
- Chandra, S., Samal, M., Chavan, V., Raghunathan, S., 2018. Hierarchical multiscale modeling of plasticity in copper: From single crystals to polycrystalline aggregates. *Int. J. Plast.* 101, 188–212.
- Chen, W., Ding, X., Feng, Y., Liu, X., Liu, K., Lu, Z., Li, D., Li, Y., Liu, C., Chen, X.Q., 2018. Vacancy formation enthalpies of high-entropy FeCoCrNi alloy via first-principles calculations and possible implications to its superior radiation tolerance. *J. Mater. Sci. Technol.* 34 (2), 355–364.
- Chen, B., Li, S., Zong, H., Ding, X., Sun, J., Ma, E., 2020a. Unusual activated processes controlling dislocation motion in body-centered-cubic high-entropy alloys. *Proc. Natl. Acad. Sci.* 117 (28), 16199–16206.
- Chen, X., Wang, Q., Cheng, Z., Zhu, M., Zhou, H., Jiang, P., Zhou, L., Xue, Q., Yuan, F., Zhu, J., et al., 2021. Direct observation of chemical short-range order in a medium-entropy alloy. *Nature* 592 (7856), 712–716.
- Chen, D., Zhao, S., Sun, J., Tai, P., Sheng, Y., Yeli, G., Zhao, Y., Liu, S., Lin, W., Kai, W., et al., 2020b. Effects of minor alloying addition on he bubble formation in the irradiated FeCoNiCr-based high-entropy alloys. *J. Nucl. Mater.* 542, 152458.
- Chen, H., Zhao, Y., Zhang, J., Wang, Y., Li, G., Wu, K., Liu, G., Sun, J., 2020c. He-ion irradiation effects on the microstructure stability and size-dependent mechanical behavior of high entropy alloy/Cu nanotwinned nanolaminates. *Int. J. Plast.* 133, 102839.
- Cheng, Z., Sun, J., Gao, X., Wang, Y., Cui, J., Wang, T., Chang, H., 2022. Irradiation effects in high-entropy alloys and their applications. *J. Alloys Compd.* 166768.
- Cho, J., Molinari, J.F., Anciaux, G., 2017. Mobility law of dislocations with several character angles and temperatures in FCC aluminum. *Int. J. Plast.* 90, 66–75.
- Cui, W., Cui, Y., Liu, W., 2021. A statistical model of irradiation hardening induced by non-periodic irradiation defects. *Scr. Mater.* 201, 113959.
- Cui, Y., Po, G., Ghoniem, N., 2017. Does irradiation enhance or inhibit strain bursts at the submicron scale? *Acta Mater.* 132, 285–297.
- Cui, Y., Po, G., Ghoniem, N.M., 2018a. A coupled dislocation dynamics-continuum barrier field model with application to irradiated materials. *Int. J. Plast.* 104, 54–67.
- Cui, Y., Po, G., Ghoniem, N., 2018b. Size-tuned plastic flow localization in irradiated materials at the submicron scale. *Phys. Rev. Lett.* 120 (21), 215501.
- Das, S., Yu, H., Mizohata, K., Tarleton, E., Hofmann, F., 2020. Modified deformation behaviour of self-ion irradiated tungsten: A combined nano-indentation, HR-EBSD and crystal plasticity study. *Int. J. Plast.* 135, 102817.
- Deluigi, O., Pasianot, R., Valencia, F., Caro, A., Farkas, D., Bringa, E., 2021. Simulations of primary damage in a high entropy alloy: Probing enhanced radiation resistance. *Acta Mater.* 213, 116951.
- Díaz de la Rubia, T., Zbib, H.M., Khraishi, T.A., Wirth, B.D., Victoria, M., Caturla, M.J., 2000. Multiscale modelling of plastic flow localization in irradiated materials. *Nature* 406 (6798), 871–874.
- Ding, Q., Zhang, Y., Chen, X., Fu, X., Chen, D., Chen, S., Gu, L., Wei, F., Bei, H., Gao, Y., et al., 2019. Tuning element distribution, structure and properties by composition in high-entropy alloys. *Nature* 574 (7777), 223–227.
- El-Atwani, O., Li, N., Li, M., Devaraj, A., Baldwin, J., Schneider, M.M., Sobieraj, D., Wróbel, J.S., Nguyen-Manh, D., Maloy, S.A., et al., 2019. Outstanding radiation resistance of tungsten-based high-entropy alloys. *Sci. Adv.* 5 (3), eaav2002.
- Erinosho, T., Dunne, F., 2015. Strain localization and failure in irradiated zircaloy with crystal plasticity. *Int. J. Plast.* 71, 170–194.
- Fan, H., Wang, Q., El-Awady, J.A., Raabe, D., Zaiser, M., 2021. Strain rate dependency of dislocation plasticity. *Nature Commun.* 12 (1), 1–11.
- Fang, Q., Li, L., Li, J., Wu, H., Huang, Z., Liu, B., Liu, Y., Liaw, P.K., 2019. A statistical theory of probability-dependent precipitation strengthening in metals and alloys. *J. Mech. Phys. Solids* 122, 177–189.
- Fang, Q., Peng, J., Chen, Y., Li, L., Feng, H., Li, J., Jiang, C., Liaw, P.K., 2021. Hardening behaviour in the irradiated high entropy alloy. *Mech. Mater.* 155, 103744.
- Feng, R., Feng, B., Gao, M.C., Zhang, C., Neufeind, J.C., Poplawsky, J.D., Ren, Y., An, K., Widom, M., Liaw, P.K., 2021. Superior high-temperature strength in a supersaturated refractory high-entropy alloy. *Adv. Mater.* 33 (48), 2102401.
- Gallagher, P., 1970. The influence of alloying, temperature, and related effects on the stacking fault energy. *Metall. Trans.* 1 (9), 2429–2461.
- Ghoniem, N., Tong, S.H., Singh, B., Sun, L., 2001. On dislocation interaction with radiation-induced defect clusters and plastic flow localization in FCC metals. *Phil. Mag. A* 81 (11), 2743–2764.
- Gururaj, K., Robertson, C., Fivel, M., 2015. Channel formation and multiplication in irradiated FCC metals: A 3D dislocation dynamics investigation. *Phil. Mag.* 95 (12), 1368–1389.
- He, M.R., Wang, S., Jin, K., Bei, H., Yasuda, K., Matsumura, S., Higashida, K., Robertson, I.M., 2016. Enhanced damage resistance and novel defect structure of CrFeCoNi under *in situ* electron irradiation. *Scr. Mater.* 125, 5–9.
- Huang, S., Guan, H., Zhong, Z., Miyamoto, M., Xu, Q., 2022. Effect of he on the irradiation resistance of equiatomic CoCrFeMnNi high-entropy alloy. *J. Nucl. Mater.* 561, 153525.
- Hýtch, M., Snoeck, E., Kilaas, R., 1998. Quantitative measurement of displacement and strain fields from HREM micrographs. *Ultramicroscopy* 74 (3), 131–146.
- Jiang, L., Hu, Y.J., Sun, K., Xiu, P., Song, M., Zhang, Y., Boldman, W.L., Crespillo, M.L., Rack, P.D., Qi, L., et al., 2020. Irradiation-induced extremes create hierarchical face-/body-centered-cubic phases in nanostructured high entropy alloys. *Adv. Mater.* 32 (39), 2002652.
- Jin, K., Lu, C., Wang, L., Qu, J., Weber, W., Zhang, Y., Bei, H., 2016. Effects of compositional complexity on the ion-irradiation induced swelling and hardening in Ni-containing equiatomic alloys. *Scr. Mater.* 119, 65–70.
- Kumar, N.K., Li, C., Leonard, K., Bei, H., Zinkle, S., 2016. Microstructural stability and mechanical behavior of FeNiMnCr high entropy alloy under ion irradiation. *Acta Mater.* 113, 230–244.
- Laplanche, G., Gadaud, P., Bärsch, C., Demtröder, K., Reinhart, C., Schreuer, J., George, E., 2018. Elastic moduli and thermal expansion coefficients of medium-entropy subsystems of the CrMnFeCoNi high-entropy alloy. *J. Alloys Compd.* 746, 244–255.
- Lee, E., Yoo, M., Byun, T., Hunn, J., Farrell, K., Mansur, L., 2001. On the origin of deformation microstructures in austenitic stainless steel: Part II—Mechanisms. *Acta Mater.* 49 (16), 3277–3287.
- Lehtinen, A., Laurson, L., Granberg, F., Nordlund, K., Alava, M.J., 2018. Effects of precipitates and dislocation loops on the yield stress of irradiated iron. *Sci. Rep.* 8 (1), 1–12.
- Lei, Z., Liu, X., Wu, Y., Wang, H., Jiang, S., Wang, S., Hui, X., Wu, Y., Gault, B., Kontis, P., et al., 2018. Enhanced strength and ductility in a high-entropy alloy via ordered oxygen complexes. *Nature* 563 (7732), 546–550.
- Li, J., Chen, H., Fang, Q., Jiang, C., Liu, Y., Liaw, P.K., 2020. Unraveling the dislocation–precipitate interactions in high-entropy alloys. *Int. J. Plast.* 133, 102819.
- Li, J., Chen, Y., He, Q., Xu, X., Wang, H., Jiang, C., Liu, B., Fang, Q., Liu, Y., Yang, Y., et al., 2022. Heterogeneous lattice strain strengthening in severely distorted crystalline solids. *Proc. Natl. Acad. Sci.* 119 (25), e2200607119.

- Li, J., Fang, Q., Liaw, P.K., 2021a. Microstructures and properties of high-entropy materials: Modeling, simulation, and experiments. *Adv. Eng. Mater.* 23 (1), 2001044.
- Li, J., Gao, B., Tang, S., Liu, B., Liu, Y., Wang, Y., Wang, J., 2018. High temperature deformation behavior of carbon-containing FeCoCrNiMn high entropy alloy. *J. Alloys Compd.* 747, 571–579.
- Li, C., Hu, X., Yang, T., Kumar, N.K., Wirth, B.D., Zinkle, S.J., 2019a. Neutron irradiation response of a Co-free high entropy alloy. *J. Nucl. Mater.* 527, 151838.
- Li, Z., Liu, Z., Zhuang, Z., Cui, Y., 2021b. Temperature dependent deformation localization in irradiated tungsten. *Int. J. Plast.* 146, 103077.
- Li, Q.J., Sheng, H., Ma, E., 2019b. Strengthening in multi-principal element alloys with local-chemical-order roughened dislocation pathways. *Nature Commun.* 10 (1), 1–11.
- Lin, Y., Yang, T., Lang, L., Shan, C., Deng, H., Hu, W., Gao, F., 2020. Enhanced radiation tolerance of the Ni-Co-Cr-Fe high-entropy alloy as revealed from primary damage. *Acta Mater.* 196, 133–143.
- Liu, W., Chen, L., Yu, L., Fu, J., Duan, H., 2022. Continuum modeling of dislocation channels in irradiated metals based on stochastic crystal plasticity. *Int. J. Plast.* 151, 103211.
- Lu, C., Niu, L., Chen, N., Jin, K., Yang, T., Xiu, P., Zhang, Y., Gao, F., Bei, H., Shi, S., et al., 2016. Enhancing radiation tolerance by controlling defect mobility and migration pathways in multicomponent single-phase alloys. *Nature Commun.* 7 (1), 1–8.
- Lu, S., Zhang, B., Li, X., Zhao, J., Zaizer, M., Fan, H., Zhang, X., 2019. Grain boundary effect on nanoindentation: A multiscale discrete dislocation dynamics model. *J. Mech. Phys. Solids* 126, 117–135.
- Ma, E., 2020. Unusual dislocation behavior in high-entropy alloys. *Scr. Mater.* 181, 127–133.
- Natarajan, V., Karunanidhi, M., Raja, B., 2020. A critical review on radioactive waste management through biological techniques. *Environ. Sci. Pollut. Res.* 27 (24), 29812–29823.
- Owen, L.R., Jones, N.G., 2018. Lattice distortions in high-entropy alloys. *J. Mater. Res.* 33 (19), 2954–2969.
- Pan, Q., Zhang, L., Feng, R., Lu, Q., An, K., Chuang, A.C., Poplawsky, J.D., Liaw, P.K., Lu, L., 2021. Gradient cell-structured high-entropy alloy with exceptional strength and ductility. *Science* 374 (6570), 984–989.
- Pei, Z., Dutta, B., Körmann, F., Chen, M., 2021. Hidden effects of negative stacking fault energies in complex concentrated alloys. *Phys. Rev. Lett.* 126 (25), 255502.
- Peng, S., Jin, K., Yi, X., Dong, Z., Guo, X., Liu, Y., Cheng, Y., Jia, N., Duan, H., Xue, J., 2022. Mechanical behavior of the HfNbZrTi high entropy alloy after ion irradiation based on micro-pillar compression tests. *J. Alloys Compd.* 892, 162043.
- Peng, J., Li, L., Li, F., Liu, B., Zhrebtssov, S., Fang, Q., Li, J., Stepanov, N., Liu, Y., Liu, F., et al., 2021. The predicted rate-dependent deformation behaviour and multistage strain hardening in a model heterostructured body-centered cubic high entropy alloy. *Int. J. Plast.* 145, 103073.
- Pickering, E.J., Carruthers, A.W., Barron, P.J., Middleburgh, S.C., Armstrong, D.E., Gandy, A.S., 2021. High-entropy alloys for advanced nuclear applications. *Entropy* 23 (1), 98.
- Pitike, K.C., Ke, H., Edwards, D.J., Setyawan, W., 2022. Helium interaction with solutes and impurities in neutron-irradiated nanostructured ferritic alloys: A first principles study. *J. Nucl. Mater.* 566, 153771.
- Po, G., Ghoniem, N., 2013. Continuum modeling of plastic flow localization in irradiated FCC metals. *J. Nucl. Mater.* 442 (1–3), S607–S611.
- Rao, S., Woodward, C., Akdim, B., Antillon, E., Parthasarathy, T., El-Awady, J., Dimiduk, D., 2019. Large-scale dislocation dynamics simulations of strain hardening of Ni microcrystals under tensile loading. *Acta Mater.* 164, 171–183.
- Ren, X., Yao, B., Zhu, T., Zhong, Z., Wang, Y., Cao, X., Jinno, S., Xu, Q., 2020. Effect of irradiation on randomness of element distribution in CoCrFeMnNi equiatomic high-entropy alloy. *Intermetallics* 126, 106942.
- Rodney, D., 2004. Molecular dynamics simulation of screw dislocations interacting with interstitial frank loops in a model FCC crystal. *Acta Mater.* 52 (3), 607–614.
- Sadeghilaridjani, M., Ayyagari, A., Muskeri, S., Hasannaeimi, V., Salloom, R., Chen, W.Y., Mukherjee, S., 2020. Ion irradiation response and mechanical behavior of reduced activity high entropy alloy. *J. Nucl. Mater.* 529, 151955.
- Shao, B., Shan, D., Guo, B., Zong, Y., 2019. Plastic deformation mechanism and interaction of B2, α 2, and O phases in Ti22Al25Nb alloy at room temperature. *Int. J. Plast.* 113, 18–34.
- Shen, S., Chen, F., Tang, X., Lin, J., Ge, G., Liu, J., 2020. Effects of carbon doping on irradiation resistance of Fe38Mn40Ni11Al4Cr7 high entropy alloys. *J. Nucl. Mater.* 540, 152380.
- Shen, Y., Spearot, D.E., 2021. Mobility of dislocations in FeNiCrCoCu high entropy alloys. *Modelling Simul. Mater. Sci. Eng.* 29 (8), 085017.
- Shi, P., Li, R., Li, Y., Wen, Y., Zhong, Y., Ren, W., Shen, Z., Zheng, T., Peng, J., Liang, X., et al., 2021. Hierarchical crack buffering triples ductility in eutectic herringbone high-entropy alloys. *Science* 373 (6557), 912–918.
- Shih, M., Miao, J., Mills, M., Ghazisaeidi, M., 2021. Stacking fault energy in concentrated alloys. *Nature Commun.* 12 (1), 1–10.
- Sills, R.B., Bertin, N., Aghaei, A., Cai, W., 2018. Dislocation networks and the microstructural origin of strain hardening. *Phys. Rev. Lett.* 121 (8), 085501.
- Singh, A., Jain, A., Liermann, H., Saxena, S., 2006. Strength of iron under pressure up to 55 GPa from X-ray diffraction line-width analysis. *J. Phys. Chem. Solids* 67 (9–10), 2197–2202.
- Su, Z., Shi, T., Yang, J., Shen, H., Li, Z., Wang, S., Ran, G., Lu, C., 2022. The effect of interstitial carbon atoms on defect evolution in high entropy alloys under helium irradiation. *Acta Mater.* 233, 117955.
- Tan, Y.Y., Su, M.Y., Xie, Z.C., Chen, Z.J., Gong, Y., Zheng, L.R., Shi, Z., Mo, G., Li, Y., Li, L.W., et al., 2021. Chemical composition dependent local lattice distortions and magnetism in high entropy alloys. *Intermetallics* 129, 107050.
- Tunes, M.A., Greaves, G., Bei, H., Edmondson, P.D., Zhang, Y., Donnelly, S.E., Schön, C.G., 2021. Comparative irradiation response of an austenitic stainless steel with its high-entropy alloy counterpart. *Intermetallics* 132, 107130.
- Wang, Y., Liu, B., Yan, K., Wang, M., Kabra, S., Chiu, Y.L., Dye, D., Lee, P.D., Liu, Y., Cai, B., 2018a. Probing deformation mechanisms of a FeCoCrNi high-entropy alloy at 293 and 77 K using *in situ* neutron diffraction. *Acta Mater.* 154, 79–89.
- Wang, Q., Lu, Y., Yu, Q., Zhang, Z., 2018b. The exceptional strong face-centered cubic phase and semi-coherent phase boundary in a eutectic dual-phase high entropy alloy AlCoCrFeNi. *Sci. Rep.* 8 (1), 1–7.
- Xin, B., Zhang, A., Han, J., Zhang, J., Meng, J., 2022. Enhancing mechanical properties of the boron doped Al0.2Co1.5CrFeNi1.5Ti0.5 high entropy alloy via tuning composition and microstructure. *J. Alloys Compd.* 896, 162852.
- Xu, Q., Guan, H., Zhong, Z., Huang, S., Zhao, J., 2021. Irradiation resistance mechanism of the CoCrFeMnNi equiatomic high-entropy alloy. *Sci. Rep.* 11 (1), 1–8.
- Yang, L., Ge, H., Zhang, J., Xiong, T., Jin, Q., Zhou, Y., Shao, X., Zhang, B., Zhu, Z., Zheng, S., et al., 2019. High he-ion irradiation resistance of CrMnFeCoNi high-entropy alloy revealed by comparison study with Ni and 304SS. *J. Mater. Sci. Technol.* 35 (3), 300–305.
- Yang, T., Xia, S., Guo, W., Hu, R., Poplawsky, J.D., Sha, G., Fang, Y., Yan, Z., Wang, C., Li, C., et al., 2018. Effects of temperature on the irradiation responses of Al0.1CoCrFeNi high entropy alloy. *Scr. Mater.* 144, 31–35.
- Zhang, Z., Armstrong, D.E., Grant, P.S., 2022. The effects of irradiation on CrMnFeCoNi high-entropy alloy and its derivatives. *Prog. Mater. Sci.* 123, 100807.
- Zhang, Y., Wang, H., An, X., Chen, G., Sun, H., Wang, Y., 2021. Dynamic strain aging behavior of accident tolerance fuel cladding FeCrAl-based alloy for advanced nuclear energy. *J. Mater. Sci.* 56 (14), 8815–8834.
- Zhang, X., Xu, Y., Jackson, R.L., 2017. An analysis of generated fractal and measured rough surfaces in regards to their multi-scale structure and fractal dimension. *Tribol. Int.* 105, 94–101.

- Zhao, Y., Lei, Z., Lu, Z., Huang, J., Nieh, T., 2019. A simplified model connecting lattice distortion with friction stress of Nb-based equiatomic high-entropy alloys. *Mater. Res. Lett.* 7 (8), 340–346.
- Zhao, S., Zhang, Y., Weber, W.J., 2022. Engineering defect energy landscape of CoCrFeNi high-entropy alloys by the introduction of additional dopants. *J. Nucl. Mater.* 561, 153573.